Supplementary Information

# Dynamic molecular pockets on diffusion channel for efficient production of polymer-grade propylene

**Table of Contents**

## Crystallographic Information

**Supplementary Table 1.** Crystal data of as-synthesized XXU-3, XXU-3a, $C_3H_6$@XXU-3a, and $C_3H_8$@XXU-3a.

| | **as-synthesized XXU-3** | **XXU-3a** | **$C_3H_6$@XXU-3a** | **$C_3H_8$@XXU-3a** | **XXU-3a** |
|---|---|---|---|---|---|
| **Temperature** | 150 K | 150 K | 150 K | 100 K | 298 K |
| **Formula** | $C_{16}H_{10}CoN_4O_4$[+solvent] | $C_{16}H_{10}CoN_4O_4$ | $C_{16}H_{10}CoN_4O_4$[+$C_3H_6$] | $C_{16}H_{10}CoN_4O_4$[+$C_3H_8$] | $C_{16}H_{10}CoN_4O_4$ |
| **CCDC number** | 2018164 | 2018163 | 2018165 | 2018166 | 2018167 |
| **Space group** | *P* $2_1$/c | *P* $2_1$/c | *P* $2_1$/c | *P* $2_1$/c | *P* $2_1$/c |
| **Crystal system** | monoclinic | monoclinic | monoclinic | monoclinic | monoclinic |
| **a (Å)** | 10.13(2) | 10.13(1) | 10.21(16) | 10.21(3) | 10.21(2) |
| **b (Å)** | 9.51 (2) | 9.43 (1) | 10.23(3) | 10.26(5) | 9.50(3) |
| **c (Å)** | 19.37(4) | 19.42(2) | 18.95(5) | 18.85(6) | 19.41(5) |
| **α (deg)** | 90 | 90 | 90 | 90 | 90 |
| **β (deg)** | 95.81(2) | 95.80(1) | 97.38(17) | 97.12(3) | 95.63(2) |
| **γ (deg)** | 90 | 90 | 90 | 90 | 90 |
| **V $(Å)^3$** | 1855.93(7) | 1846.01(3) | 1963.72(8) | 1961.46(13) | 1872.93(8) |
| **Z** | 4 | 4 | 4 | 4 | 4 |
| **ρ calcg/$cm^3$** | 1.593 | 1.372 | 1.432 | 1.440 | 1.352 |
| **μ/$mm^{-1}$** | 7.752 | 7.530 | 7.135 | 7.143 | 7.422 |
| **Final R [I>2sigma (I)]** | R1=0.0553<br>wR1=0.1606 | R1=0.0551<br>wR1=0.1560 | R1=0.0782<br>wR1=0.2198 | R1=0.0695<br>wR1=0.2065 | R1=0.0531<br>wR1=0.1635 |
| **GooF** | 1.084 | 0.999 | 1.040 | 1.039 | 1.123 |
| **Completeness** | 100% | 100% | 100% | 100% | 100% |

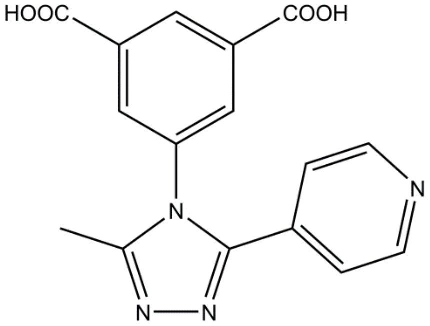

**Supplementary Figure 1.** The structure of 5-(3-methyl-5-(pyridin-4-yl)-4H-1,2,4-triazol-4-yl)-1,3-benzenedicarboxylic acid ($H_2MPTBDC$).

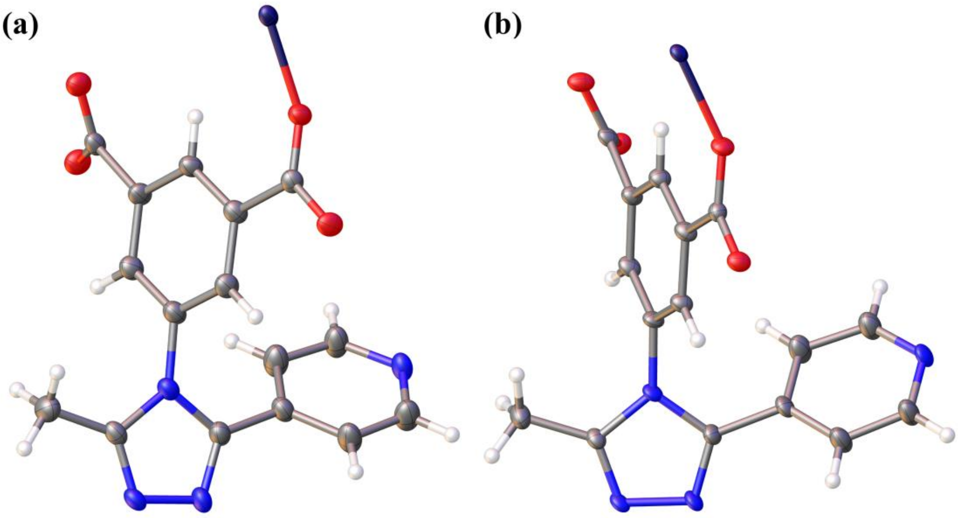

**Supplementary Figure 2.** The local coordination environments of (a) as-synthesized and (b) desolvated XXU-3. (Co, light blue; C, dark grey; N, blue; O, red; H, white).

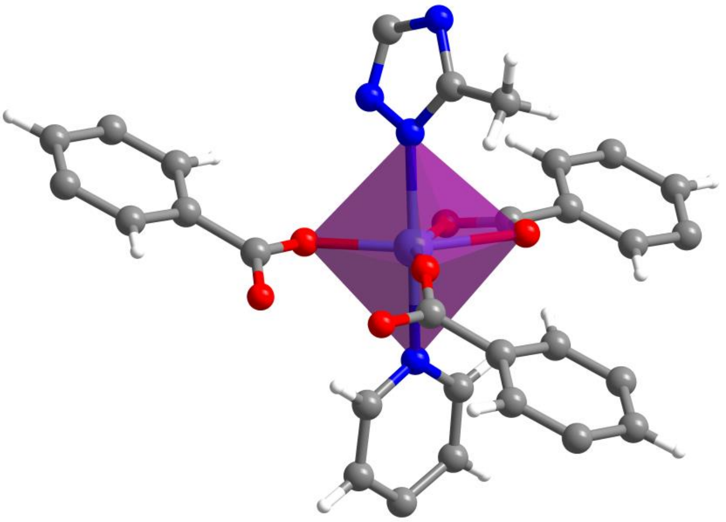

**Supplementary Figure 3.** Local coordination environment of Co$^{2+}$. (Co, light blue; C, dark grey; N, blue; O, red; H, white).

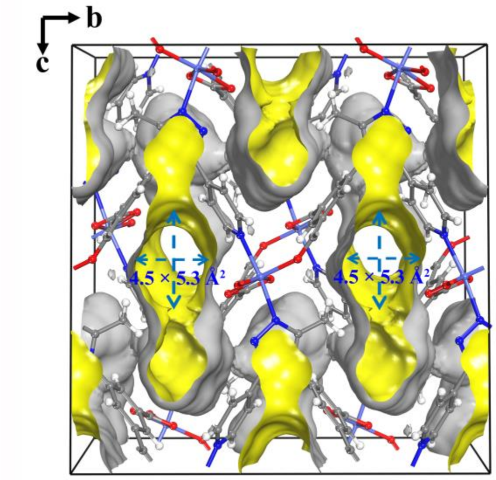

**Supplementary Figure 4.** Connolly surface representation of XXU-3 viewed along the *a*-axis (yellow/gray curved surface).

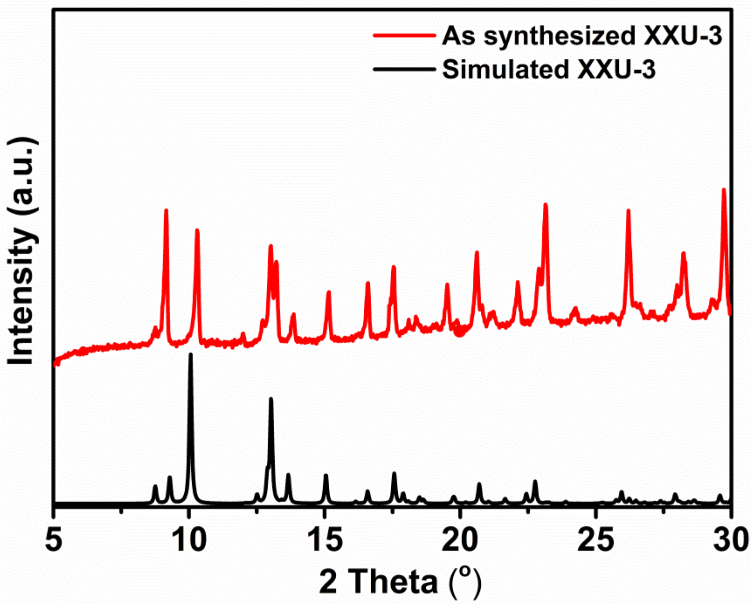

**Supplementary Figure 5.** PXRD patterns of the simulated (black) and as-synthesized (red) XXU-3.

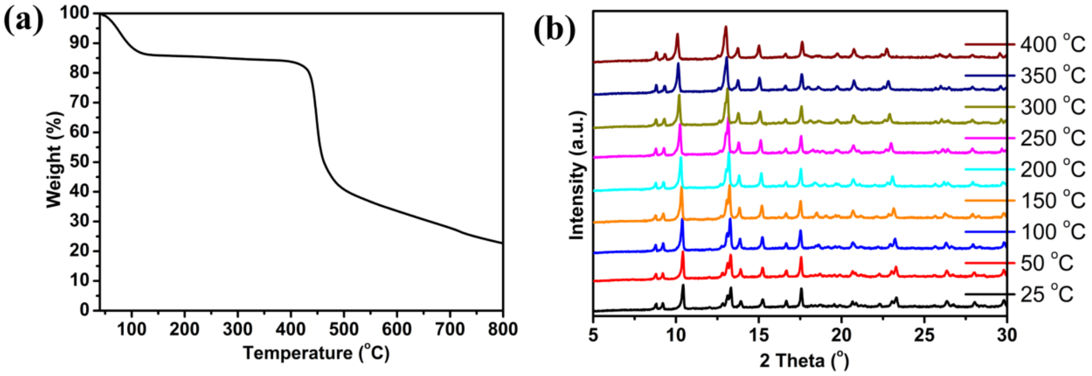

**Supplementary Figure 6.** (a) Thermogravimetric analysis (TGA) curve of XXU-3a. (b) *In-situ* variable-temperature PXRD (VT-PXRD) patterns of XXU-3a under a $N_2$ atmosphere.

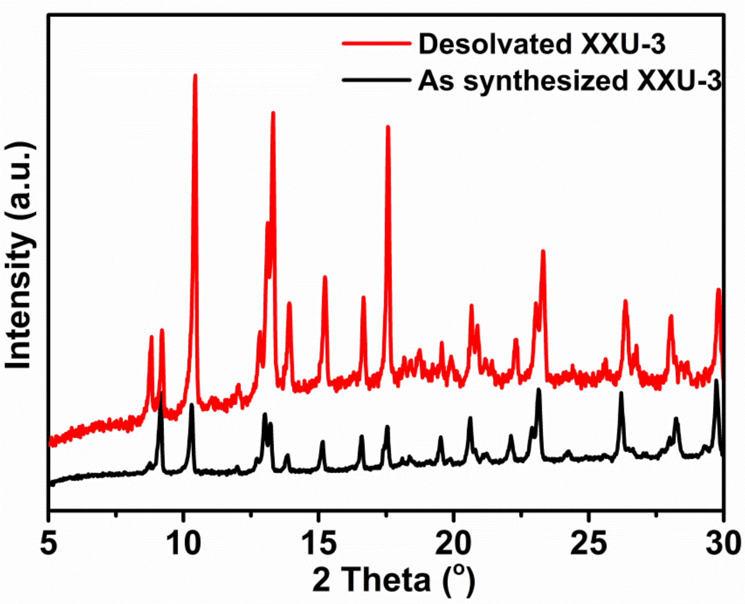

**Supplementary Figure 7.** PXRD patterns of the as-synthesized (black) and desolvated (red) XXU-3.

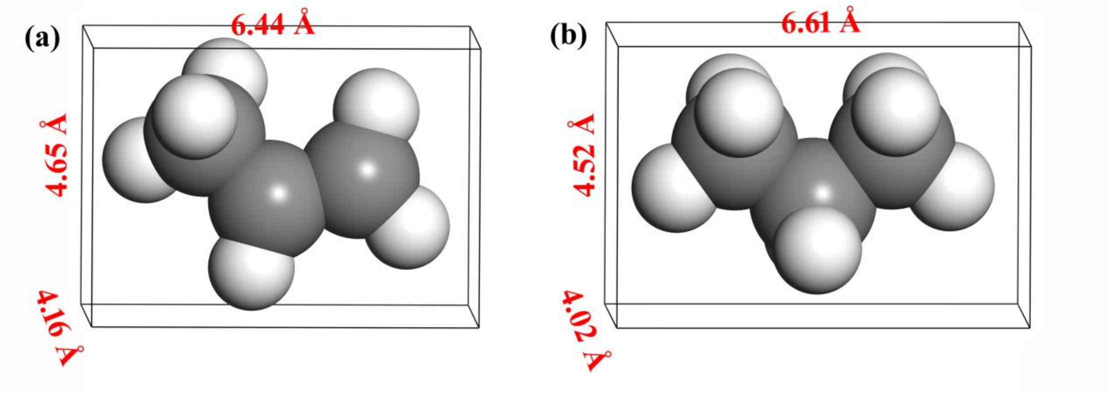

**Supplementary Figure 8.** Molecular dimensions of (a) $C_3H_6$ and (b) $C_3H_8$[3].

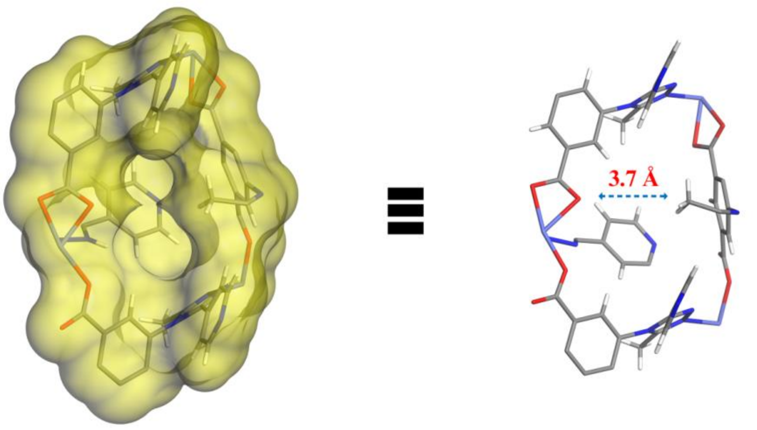

**Supplementary Figure 9.** Close-up view of the "gourd-shaped" aperture connecting the pocket to the channel. Color code: light blue, Co; red, O; blue, N; white, H; and grey, C atoms.

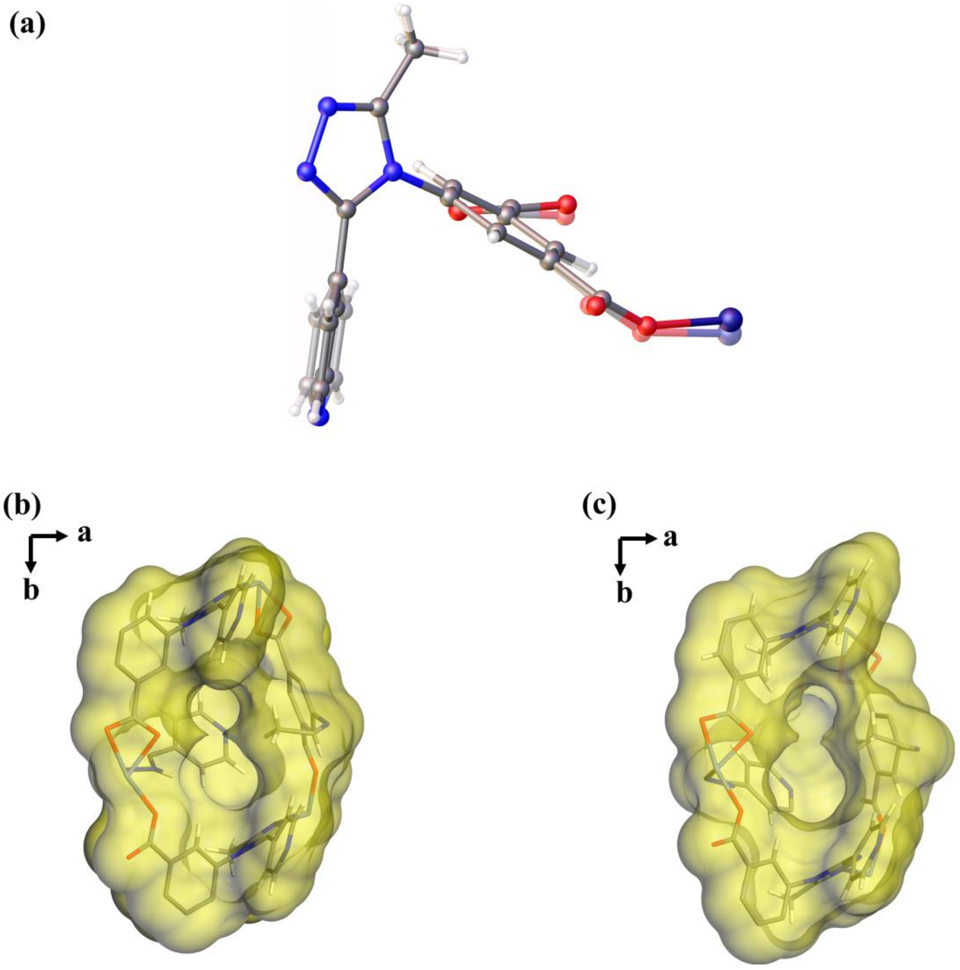

**Supplementary Figure 10.** (a) Conformations of the MPTBDC linkers in the crystal structures of XXU-3a at 150 K and 298 K. Connolly surface representation of the dynamic single molecular pocket with a "gourd-shaped" aperture at 150 K (b) and 298 K (c).

## Single-Component Gas Adsorption Isotherm Measurements

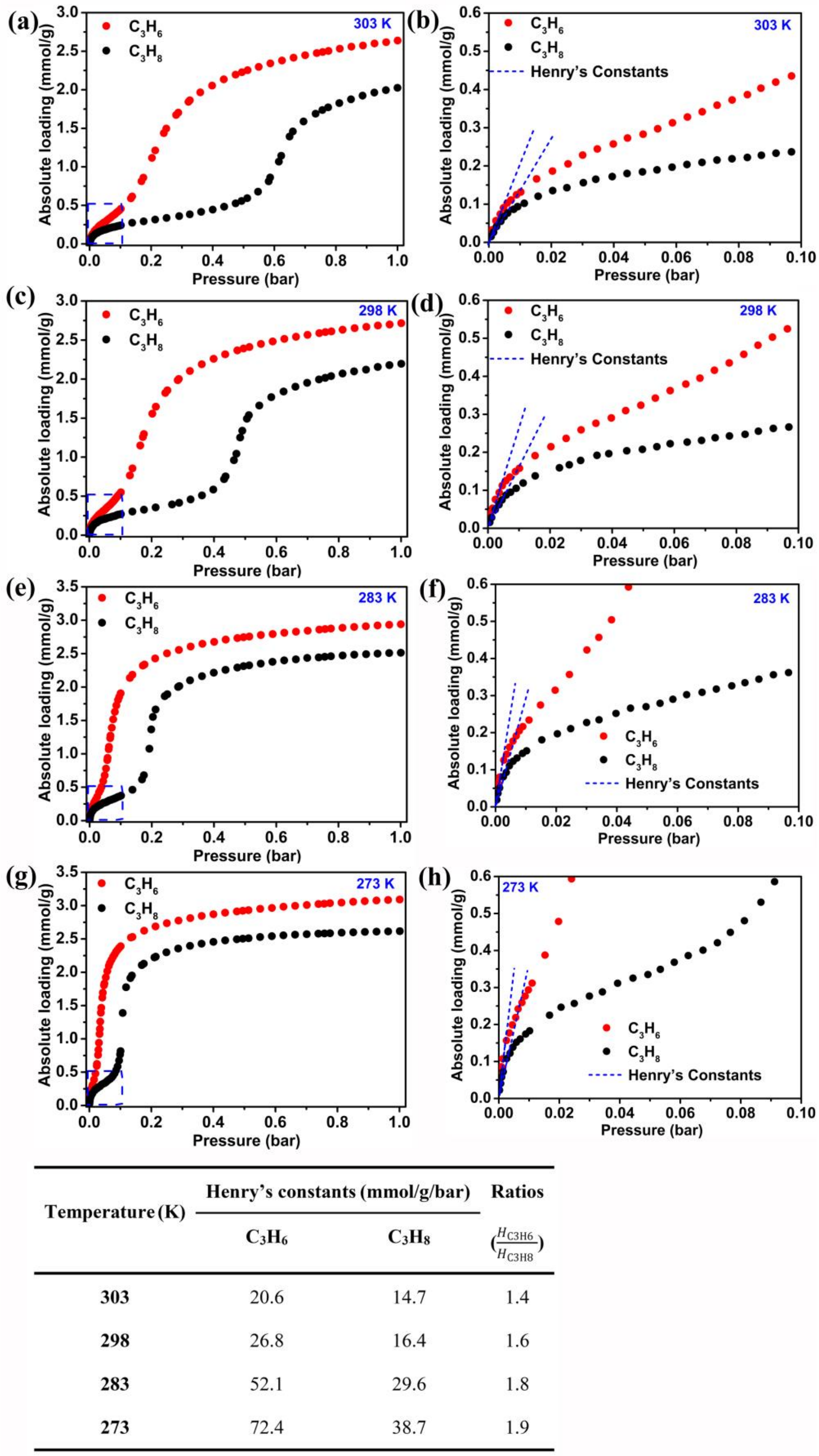

| Temperature (K) | Henry's constants (mmol/g/bar) | | Ratios |
|---|---|---|---|
| | $C_3H_6$ | $C_3H_8$ | $(\frac{H_{C3H6}}{H_{C3H8}})$ |
| **303** | 20.6 | 14.7 | 1.4 |
| **298** | 26.8 | 16.4 | 1.6 |
| **283** | 52.1 | 29.6 | 1.8 |
| **273** | 72.4 | 38.7 | 1.9 |

**Supplementary Figure 11.** $C_3H_6$ and $C_3H_8$ adsorption isotherms of XXU-3a at different temperatures and the zoomed-in pre-step adsorption at low pressures. Summary of the Henry's constants for $C_3H_6$ and $C_3H_8$ at different temperatures.

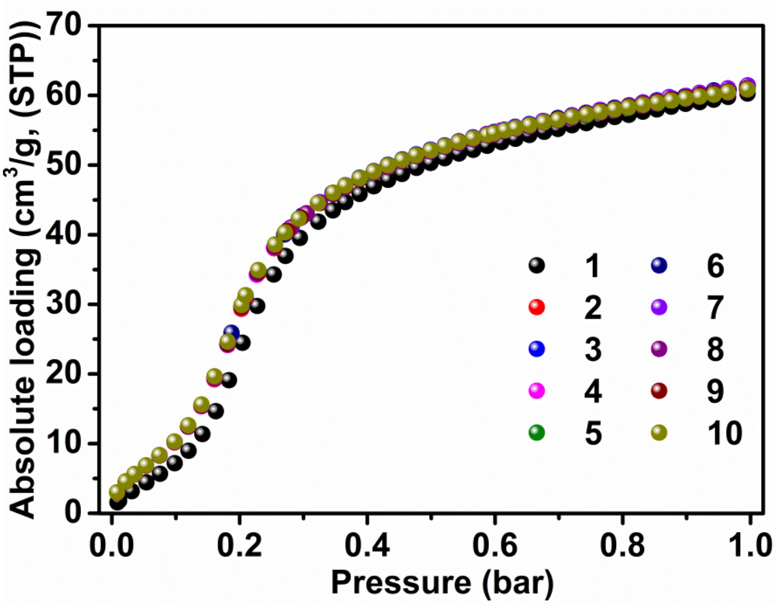

**Supplementary Figure 12.** Continuous $C_3H_6$ adsorption measurements on XXU-3a at 303 K.

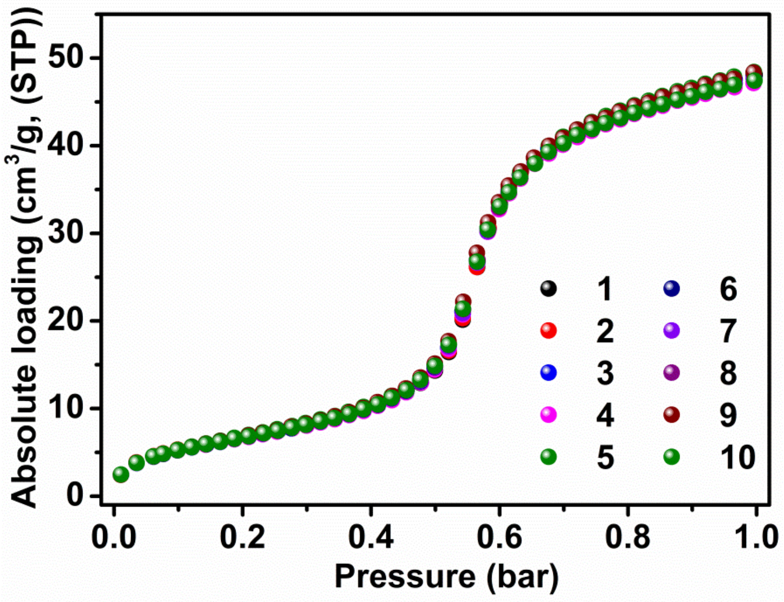

**Supplementary Figure 13.** Continuous $C_3H_8$ adsorption measurements on XXU-3a at 303 K.

## Isotherm Fitting, Differential Enthalpies, and IAST Calculations

### The isosteric enthalpy of adsorption ($Q_{st}$).

The isosteric enthalpy of adsorption for $C_3H_6$ and $C_3H_8$ were calculated by using the gas adsorption data collected at 273, 283 and 298 K. The adsorption curves were first fitted with the viral equation[1]:

$$\ln P = \ln N + \frac{1}{T}\sum_{i=0}^{m} a_i N^i + \sum_{i=0}^{n} b_i N^i$$

Where N is gas uptake (in mg $g^{-1}$), $P$ is pressure (in mmHg), a and b are virial coefficients, m and n are the numbers of coefficients require to adequately describe the isotherm. The parameters that were obtained from the fitting of the $C_3H_6$ and $C_3H_8$ adsorption isotherms can be found in **Supplementary Figs. 14 and 15**. All isotherms were fitted with $R^2 > 0.998$.

The obtained parameters were used to calculate $Q_{st}$ in the range of adsorption capacity through the virial equation, which is as follows:

$$\mathrm{Q}_{st} = -\mathrm{R}\sum_{i=0}^{m} a_i N^i$$

### IAST calculations of adsorption selectivity.

In order to establish the feasibility of $C_3H_6/C_3H_8$ separation, we performed calculations using the Ideal Adsorbed Solution Theory (IAST) of Myers and Prausnitz[2].

Adsorption selectivity, $S_{ads}$, is defined for separation of a binary mixture of species i and j by

$$S_{ads} = \frac{q_i/q_j}{p_i/p_j}$$

where $q_i$ and $q_j$ represent the molar loadings of component i and j that is in equilibrium; $p_i$ and $p_j$ represent the partial pressures of component i and j in the bulk gas phase.

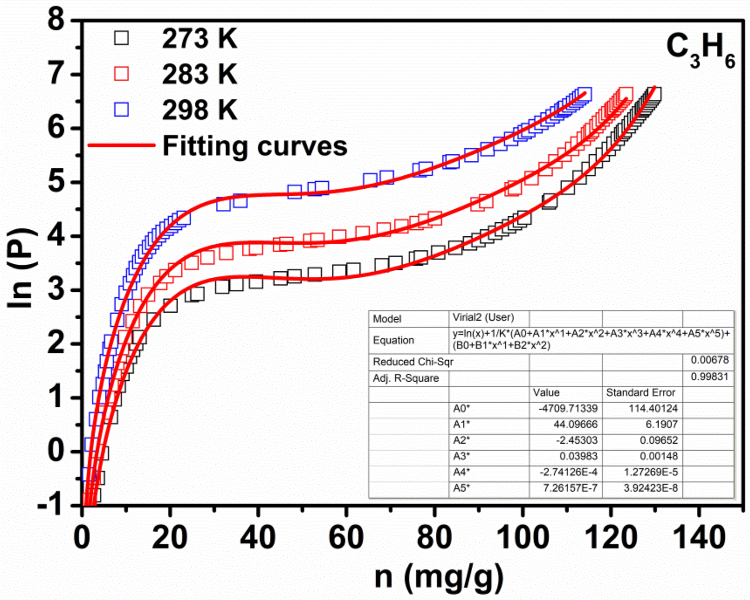

| | | | | |
|---|---|---|---|---|
| Model | Virial2 (User) | | | |
| Equation | y=ln(x)+1/K*(A0+A1*x^1+A2*x^2+A3*x^3+A4*x^4+A5*x^5)+(B0+B1*x^1+B2*x^2) | | | |
| Reduced Chi-Sqr | | | | 0.00678 |
| Adj. R-Square | | | | 0.99831 |
| | | Value | Standard Error | |
| | A0* | -4709.71339 | 114.40124 | |
| | A1* | 44.09666 | 6.1907 | |
| | A2* | -2.45303 | 0.09652 | |
| | A3* | 0.03983 | 0.00148 | |
| | A4* | -2.74126E-4 | 1.27269E-5 | |
| | A5* | 7.26157E-7 | 3.92423E-8 | |

**Supplementary Figure 14.** Virial equation fitting of the $C_3H_6$ adsorption isotherms of XXU-3a at 273 K, 283 K and 298 K.

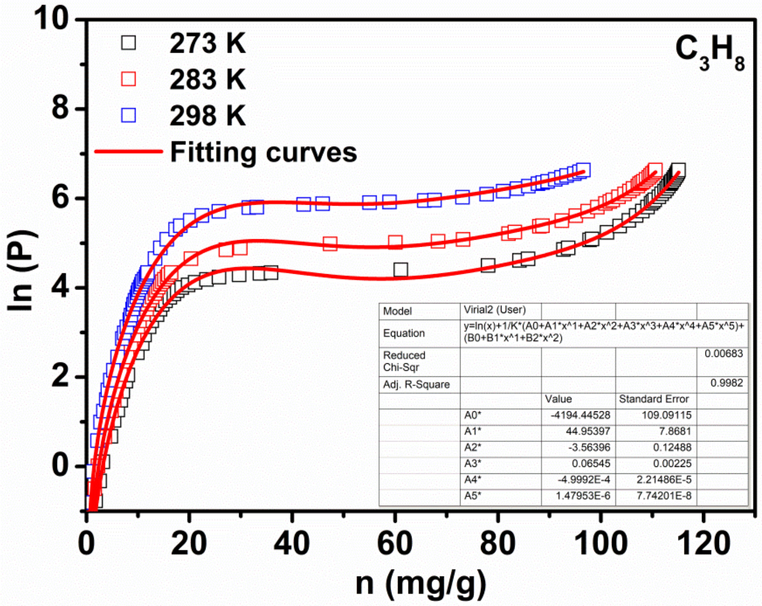

| | | | | |
|---|---|---|---|---|
| Model | Virial2 (User) | | | |
| Equation | y=ln(x)+1/K*(A0+A1*x^1+A2*x^2+A3*x^3+A4*x^4+A5*x^5)+(B0+B1*x^1+B2*x^2) | | | |
| Reduced Chi-Sqr | | | | 0.00683 |
| Adj. R-Square | | | | 0.9982 |
| | | Value | Standard Error | |
| | A0* | -4194.44528 | 109.09115 | |
| | A1* | 44.95397 | 7.8681 | |
| | A2* | -3.56396 | 0.12488 | |
| | A3* | 0.06545 | 0.00225 | |
| | A4* | -4.9992E-4 | 2.21486E-5 | |
| | A5* | 1.47953E-6 | 7.74201E-8 | |

**Supplementary Figure 15.** Virial equation fitting of the $C_3H_8$ adsorption isotherms of XXU-3a at 273 K, 283 K and 298 K.

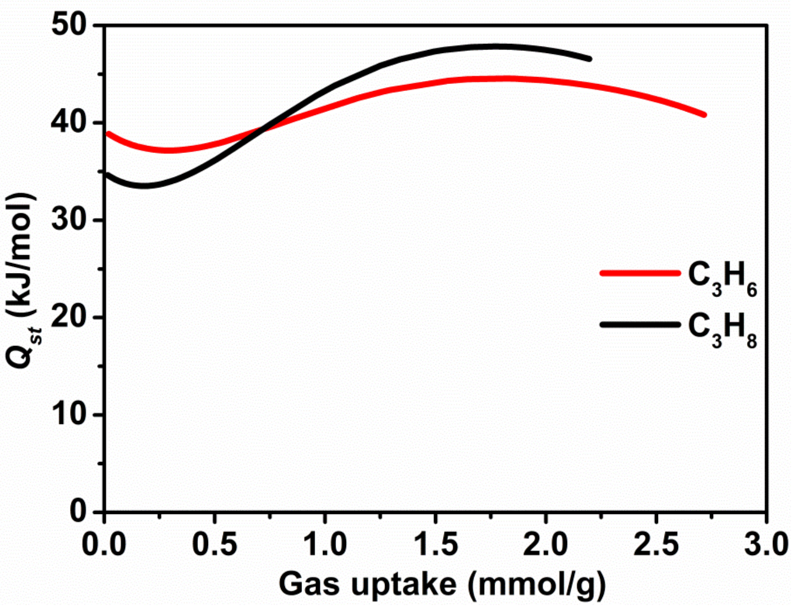

**Supplementary Figure 16.** Calculated $C_3H_6$ and $C_3H_8$ adsorption enthalpy ($Q_{st}$) of XXU-3a.

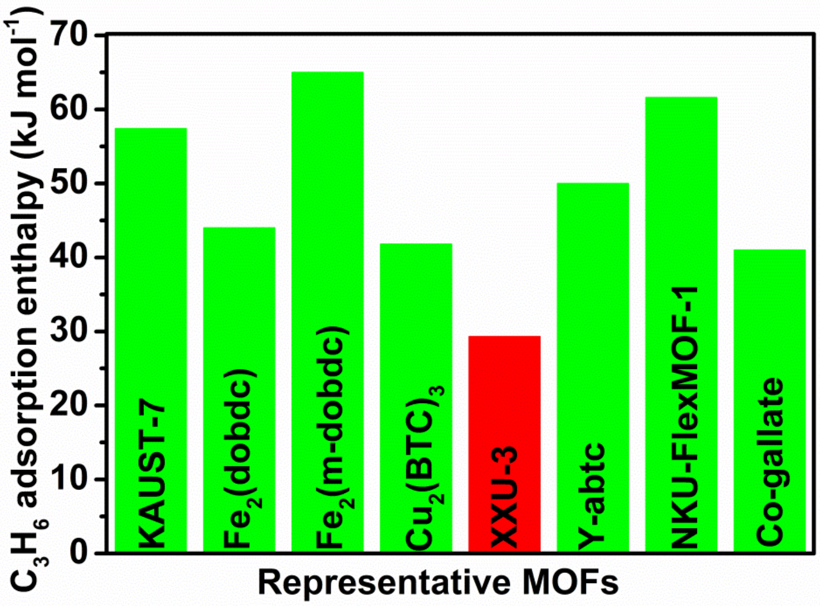

**Supplementary Figure 17.** The maximum $C_3H_6$ adsorption enthalpy of XXU-3a and some selected high-performance MOFs.

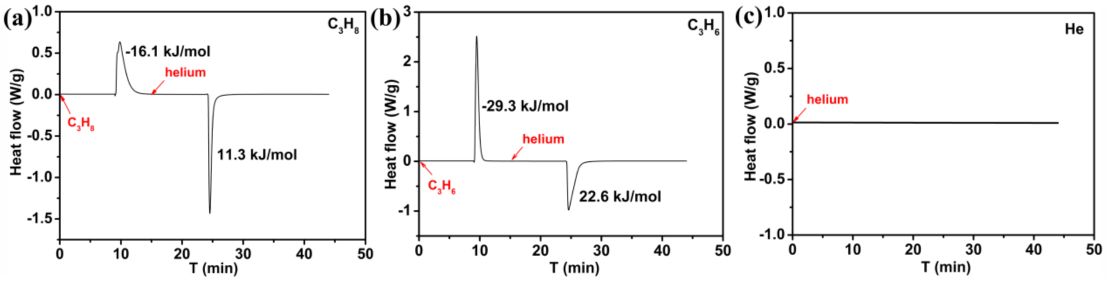

**Supplementary Figure 18.** Differential scanning calorimetry of $C_3H_8$ and $C_3H_6$ adsorption and desorption on XXU-3a at 303 K and 1 bar. The adsorption was carried out under $C_3H_8$ or $C_3H_6$ gas at a flowrate of 5.0 mL min$^{-1}$. The desorption was carried out under helium gas at a flowrate of 5.0 mL min$^{-1}$.

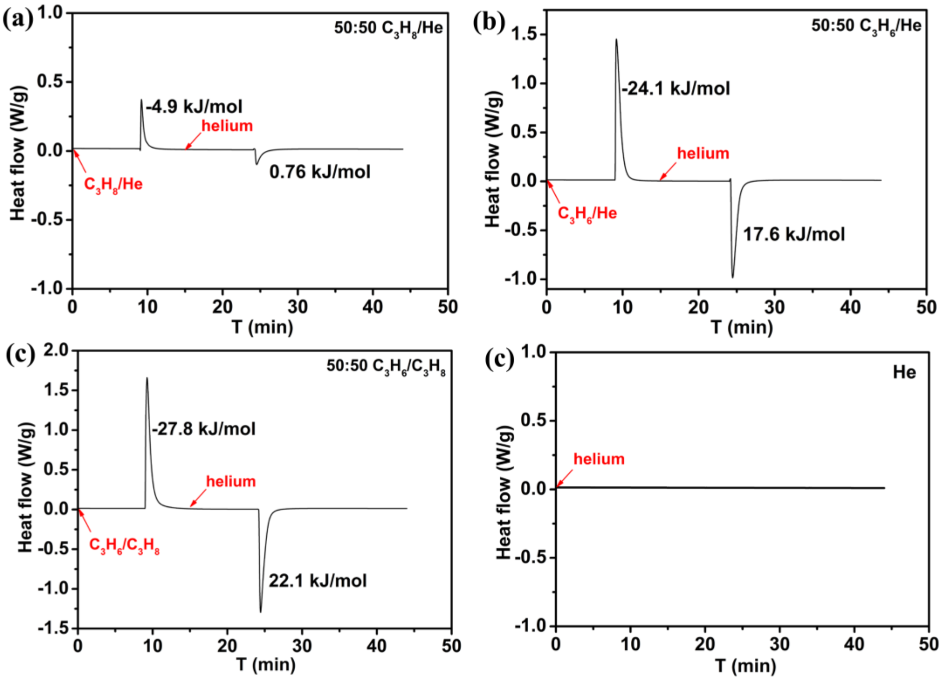

**Supplementary Figure 19.** Differential scanning calorimetry of 50/50 mixed-component ((a) $C_3H_6$/He, (b) $C_3H_8$/He, or (c) $C_3H_6$/$C_3H_8$) and (d) helium on XXU-3a at 303 K. The flowrate is 5.0 mL min$^{-1}$.

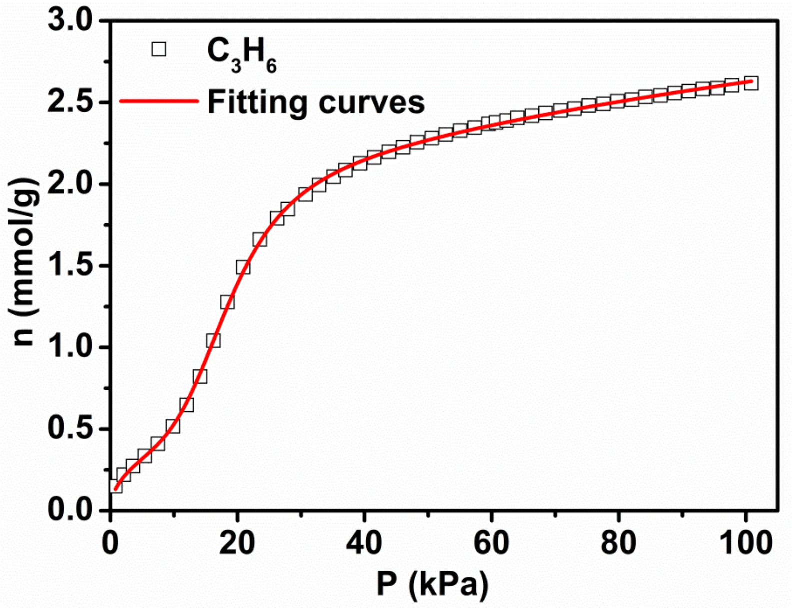

**Supplementary Figure 20.** Dual-site Langmuir-Freundlich fitting of the $C_3H_6$ adsorption isotherm of XXU-3a at 303 K.

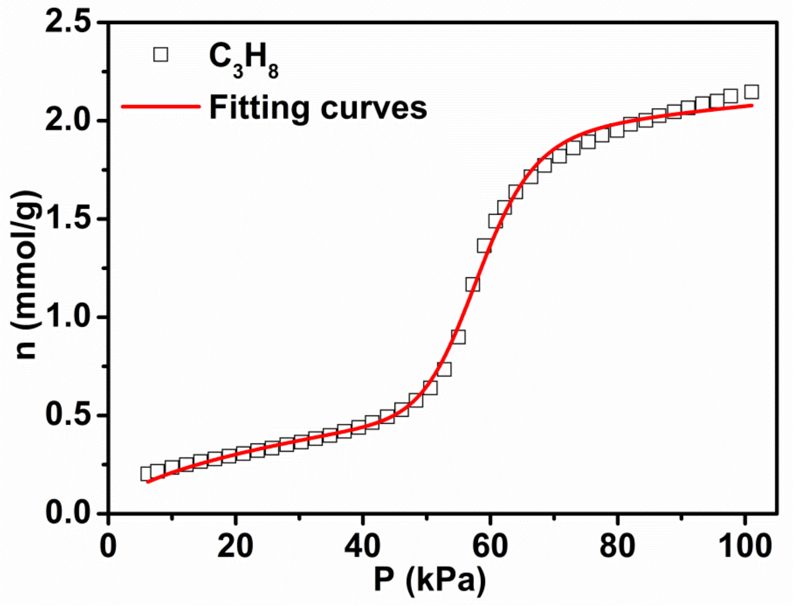

**Supplementary Figure 21.** Dual-site Langmuir-Freundlich fitting of the $C_3H_8$ adsorption isotherm of XXU-3a at 303 K.

**Supplementary Table 2.** Dual-site Langmuir-Freundlich parameters from the fitting of $C_3H_6$ and $C_3H_8$ adsorption isotherms of XXU-3a at 303 K. The $R^2$ values are also provided.

| **Parameter** | $C_3H_6$ | $C_3H_8$ |
|---|---|---|
| $q_{A,sat}$ | 23.123 | 4.800 |
| $b_A$ | 0.00639 | 0.0127 |
| $n_A$ | 2.110 | 1.795 |
| $q_{B,sat}$ | 1.386 | 1.397 |
| $b_B$ | 5.649E-6 | 4.858E-24 |
| $n_B$ | 0.242 | 0.0757 |
| $R^2$ | 0.999 | 0.998 |

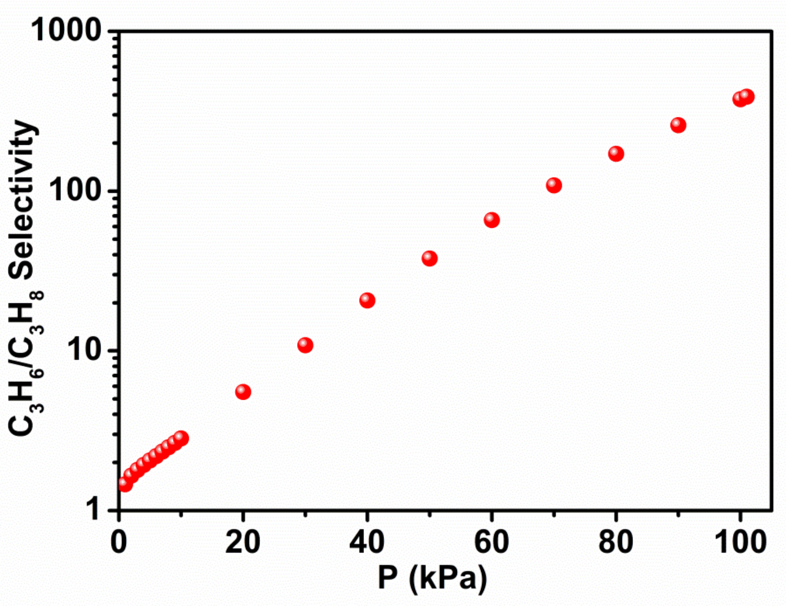

**Supplementary Figure 22.** Calculated IAST adsorption selectivity of $C_3H_6$ over $C_3H_8$ on XXU-3a for an equimolar mixture of $C_3H_6$/$C_3H_8$ at 303 K.

# Diffusion Rate and Time-Dependent Kinetic Sorption Isotherms

## Quantification of the diffusion rate

The diffusion rate was measured on a BELSORP-max II (BEL Japan, Inc.) automated volumetric sorption analyzer and was fitted automatically with BEL-Master software according to the Crank theory[4] described as follows:

Adsorption rate equation in consideration of in-particle diffusion (assuming spherical particle):

$$\frac{\partial q}{\partial t} = D_S\left(\frac{\partial^2 q}{\partial r^2} + \frac{2}{r}\frac{\partial q}{\partial r}\right) \quad (1)$$

Boundary condition: When $r = R$, $q = q_{0n}$

Linear equilibrium equation:

$$q^* = H \times P \quad (2)$$

$H$: Equilibrium constant [$m^3$ / g], $p$: Pressure [Pa]

Equation (3) for batch adsorbing operation is used.

$$W\,(q - q_0) = V\,(p_0 - p) \quad (3)$$

$W$: Mass of adsorbent [g], $V$: Fluid volume [$m^3$]

By solving simultaneous equations of the above (1), (2), and (3), the following solution is obtained:

$$\frac{p}{p_0} = 1 - \left(\frac{1}{\alpha+1}\right)\left[1 - \sum_{n=1}^{\infty}\frac{6\alpha(\alpha+1)\exp\left(-q_n^2\tau_s\right)}{9+9\alpha+q_n^2\alpha^2}\right] \quad (4)$$

Equation (4) is called "Crank equation". When Equation (4) is solved as with Equation.

$$\frac{p-p_{en}}{p_0-p_{en}} = 1 - \left(\frac{p_0-p_{en}}{p_0-p_{en}}\right)\left(\frac{1}{\alpha+1}\right)\left[1 - \sum_{n=1}^{\infty}\frac{6\alpha(\alpha+1)\exp\left(-q_n^2\tau_s\right)}{9+9\alpha+q_n^2\alpha^2}\right] \quad (5)$$

With gas state Equation ($p = cRT$), Equation (5) is expressed as the following equation, from which solution of analysis considering pore diffusion can be obtained.

$$\frac{C-C_{en}}{Cp_0-C_{en}} = 1 - \left(\frac{C_0-C_{en}}{C_0-C_{en}}\right)\left(\frac{1}{\alpha+1}\right)\left[1 - \sum_{n=1}^{\infty}\frac{6\alpha(\alpha+1)\exp\left(-q_n^2\tau_s\right)}{9+9\alpha+q_n^2\alpha^2}\right] \quad (6)$$

Wherein, $\tau_s = \frac{D}{R^2}\,t$, tan $q_n = \frac{3q_n}{3+\alpha {q_n}^2}$

## Time-dependent kinetic sorption isotherms of XXU-3a

The time-dependent kinetic adsorption isotherms were collected on Micromeritics ASAP 2020 Plus in Rate of Adsorption (ROA) mode (place roa.exe in the directory where the 2020Plus.exe is located).

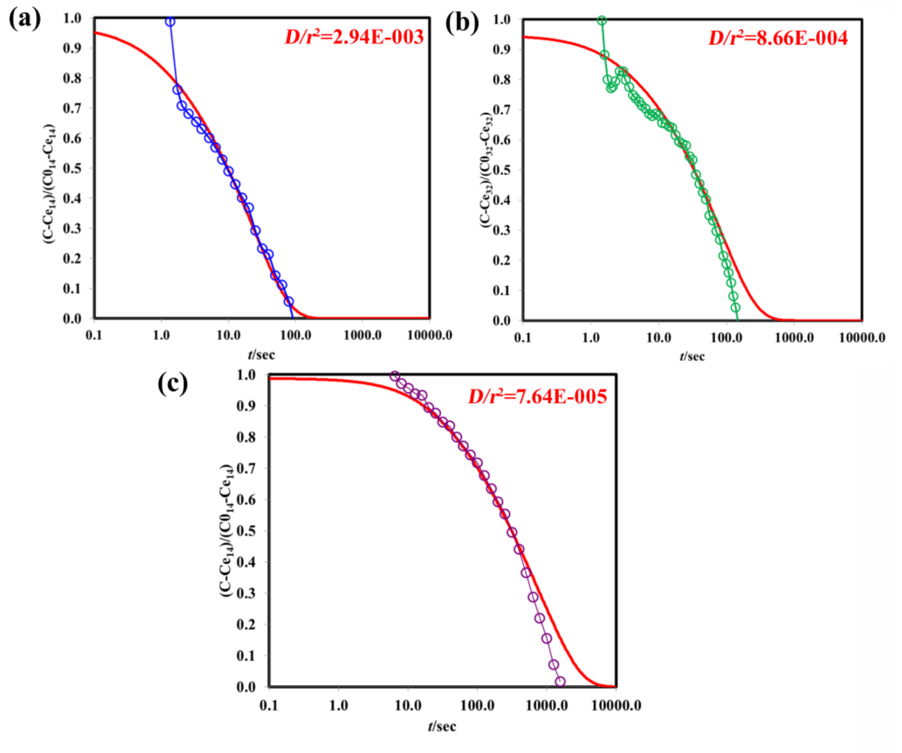

**Supplementary Figure 23.** The calculated diffusion rate of $C_3H_6$ on (a) XXU-3a, (b) KAUST-7, and (c) Y-abtc, fitted automatically with BEL-Master software according to the Crank theory 错误!未定义书签。.

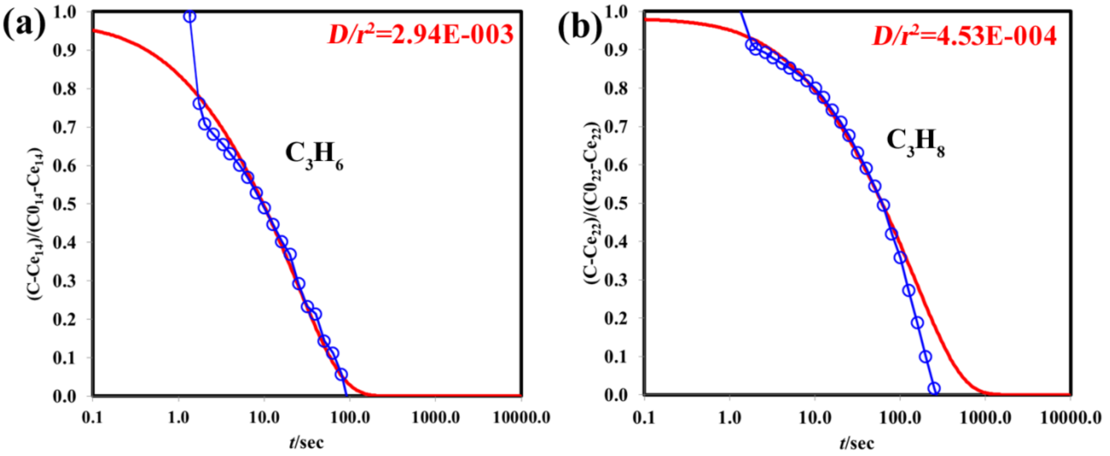

**Supplementary Figure 24.** The calculated diffusion rate of (a) $C_3H_6$ and (b) $C_3H_8$ on XXU-3a, fitted automatically with BEL-Master software according to the Crank theory[4].

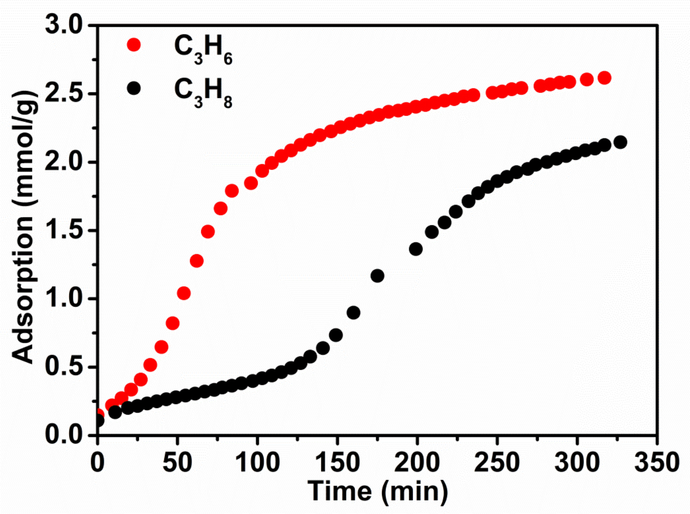

**Supplementary Figure 25.** $C_3H_6$ and $C_3H_8$ kinetic adsorption on XXU-3a at 303 K.

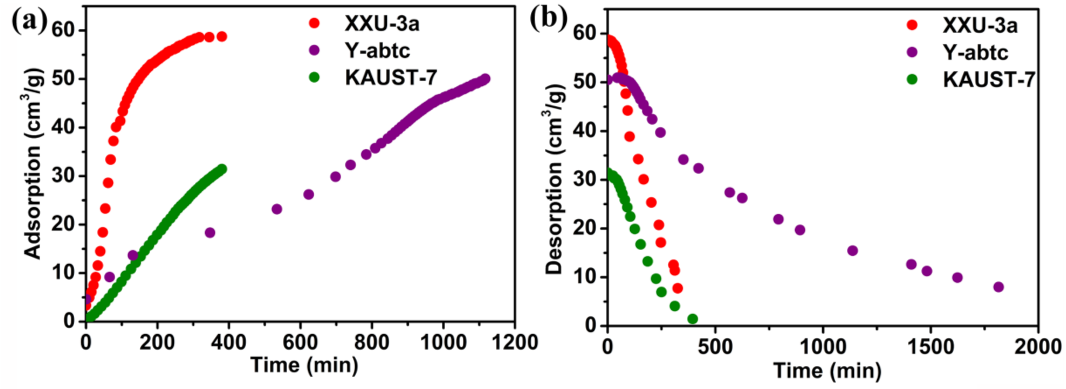

**Supplementary Figure 26. (a)** $C_3H_6$ kinetic adsorption on XXU-3a, Y-abtc, and KAUST-7 at 303 K. (b) $C_3H_6$ kinetic desorption on XXU-3a, Y-abtc, and KAUST-7 at 303 K.

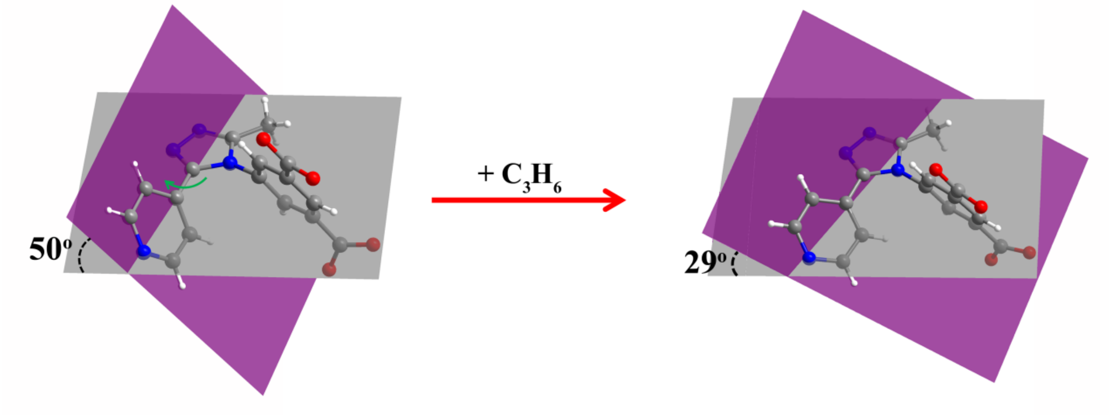

**Supplementary Figure 27.** Rotation of dihedral angle between the pyridine plane and triazole plane upon $C_3H_6$ loading. Data are from the crystal structures of XXU-3a and $C_3H_6$@XXU-3a at 150 K.

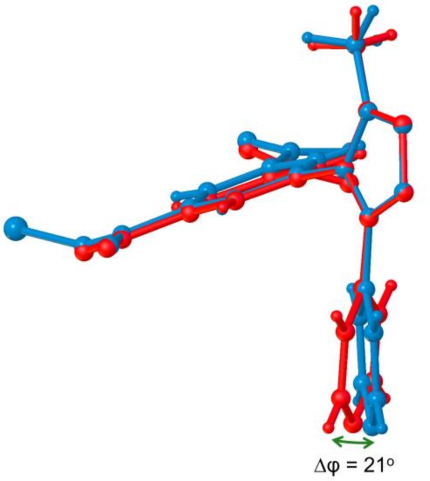

**Supplementary Figure 28.** Conformational comparison of the MPTBDC linkers in the crystal structures of XXU-3a (turquoise) and $C_3H_6$@XXU-3a (red) at 150 K.

## Additional DFT Figures and Details

### Computational details

All calculations were performed by using the density functional theory (DFT) method in Cambridge Sequential Total Energy Package (CASTEP) module embedded in Materials Studio 2018 (MS 2018). The Perdew-Burke-Ernzerhof (PBE) functional of GGA was employed in optimization and thermodynamic energy calculations. OTFG ultra-soft pseudopotentials were used to describe all atoms with an energy cutoff of 489 eV at gamma point. Geometry optimizations were performed in the unit cell using the single-crystal structure obtained from the experiment as the initial structure for XXU-3 and guest@XXU-3 model. The guest molecule was optimized in the periodic boundary conditions with the cell parameters of guest@XXU-3. The atomic positions were fully optimized followed the fine convergence standards.

The binding energy ($E_b$) of guest adsorbed in XXU-3 was calculated with the following equation:

$$E_b = \left(E_{guest@XXU-3} - E_{XXU-3} - nE_{guest}\right)/n$$

Where $E_{guest@XXU-3}$ is the total enthalpy of XXU-3 with adsorbed guest molecules per unit cell, $E_{XXU-3}$ and $E_{guest}$ are the enthalpy of empty XXU-3 and free guest molecule, respectively. Herein, the number of adsorbed molecules is four.

To find out whether all the pockets open in a cooperative manner or every pocket has to further rearrange in order to accommodate $C_3H_6$, we perform the following calculations:

1. First $C_3H_6$ molecule was put in the bottom left pocket of XXU-3a, and full relax the geometry and cell parameters of the one gas molecule adsorption model XXU-3a@1$C_3H_6$, and the energy ($\Delta E$) of $C_3H_6$ adsorbed in XXU-3a was calculated with the following equation:

$$\Delta E = E_{XXU-3a@1C3H6} - E_{XXU-3a} - E_{C3H6}$$

2. Second $C_3H_6$ molecule was put into the top left pocket of XXU-3a@1$C_3H_6$, fix the geometry and cell parameters, only the second $C_3H_6$ is optimized, and the energy ($\Delta E$) of $C_3H_6$ adsorbed in XXU-3a was calculated with the following equation:

$$\Delta E = E_{XXU-3a@2C3H6} - E_{XXU-3a@1C3H6} - E_{C3H6}$$

3. Similarly, second $C_3H_6$ molecule was put into the top left pocket of XXU-3a@1$C_3H_6$, full relax the cell parameters and geometries, and the energy ($\Delta E$) of $C_3H_6$ adsorbed in XXU-3a was calculated with the following equation:

$$\Delta E = E_{XXU-3a@2C3H6} - E_{XXU-3a@1C3H6} - E_{C3H6}$$

The electrostatic potential (ESP) calculation was performed with the Gaussian program at the cut model of the crystal structure without further optimization. The cut bond was saturated by H atoms. PBE with dispersion correction (PBE-D3)[5] and def2-TZVP[6] basis set were employed.

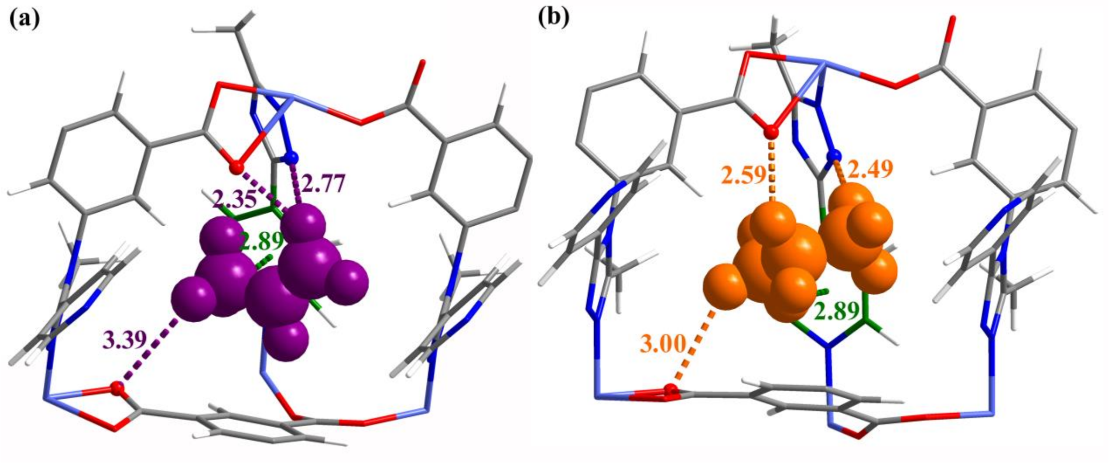

**Supplementary Figure 29.** (a) The binding configurations of (a) $C_3H_6$ and (b) $C_3H_8$ in the pockets of XXU-3a at room temperature, optimized by DFT calculations. $C_3H_6$ and $C_3H_8$ molecule are depicted in violet and orange, respectively, and distances are in Å. Color code: light blue, red, blue, white, and grey nodes represent Co, O, N, H, and C atoms, respectively.

## Breakthrough Experiments

### Column Breakthrough Experiments.

The mixed-gas breakthrough separation experiment was conducted under ambient conditions (303 K, 1 atm) by using a lab-scale fixed-bed system (**Supplementary Fig. 30**). In a typical breakthrough experiment for $C_3H_6/C_3H_8$ (50/50, mol/mol) gas mixture, XXU-3a powder (1.4 g) was packed into a custom-made stainless steel column (3.15 mm I.D. × 450 mm) with silica wool filling the void space. The sorbent was activated *in-situ* in the column at 373 K with a high vacuum for 12 h. After the activation process, a helium flow (100 $cm^3$ $min^{-1}$) was introduced to purge the adsorbent. The flow of helium was then turned off and a gas mixture of $C_3H_6/C_3H_8$ (1 $cm^3$ $min^{-1}$) was allowed to flow into the column. Outlet effluent from the column was continuously monitored using gas chromatography (GC-7890B, Agilent) with a thermal conductivity detector (TCD). After the breakthrough experiment, the sample was regenerated *in-situ* in the column at room temperature with a high vacuum or helium sweeping for 2 h. The complete breakthrough of $C_3H_6$ was indicated by the downstream gas composition reaching that of the feed gas. On the basis of the mass balance, the gas adsorption capacities can be determined as follows[6]:

$$q_i = \frac{C_i V}{22.4 \times m} \times \int_0^t (1 - \frac{F}{F_0})\, dt$$

Where $q_i$ is the equilibrium adsorption capacity of gas i (mmol $g^{-1}$), $C_i$ is the feed gas concentration, V is the volumetric feed flow rate ($cm^3$ $min^{-1}$), t is the adsorption time (min), $F_0$ and F are the inlet and outlet gas molar flow rates, respectively, and m is the mass of the adsorbent (g).

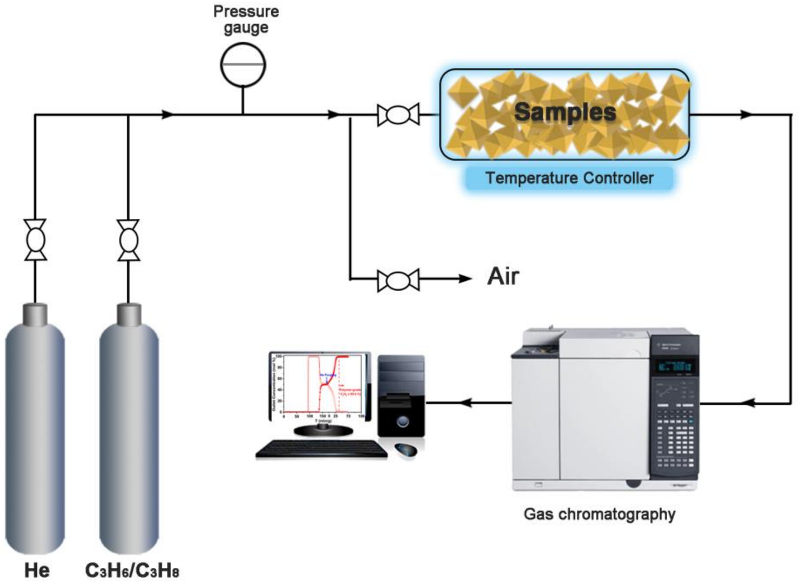

**Supplementary Figure 30**. Schematic illustration of the setup for breakthrough experiments.

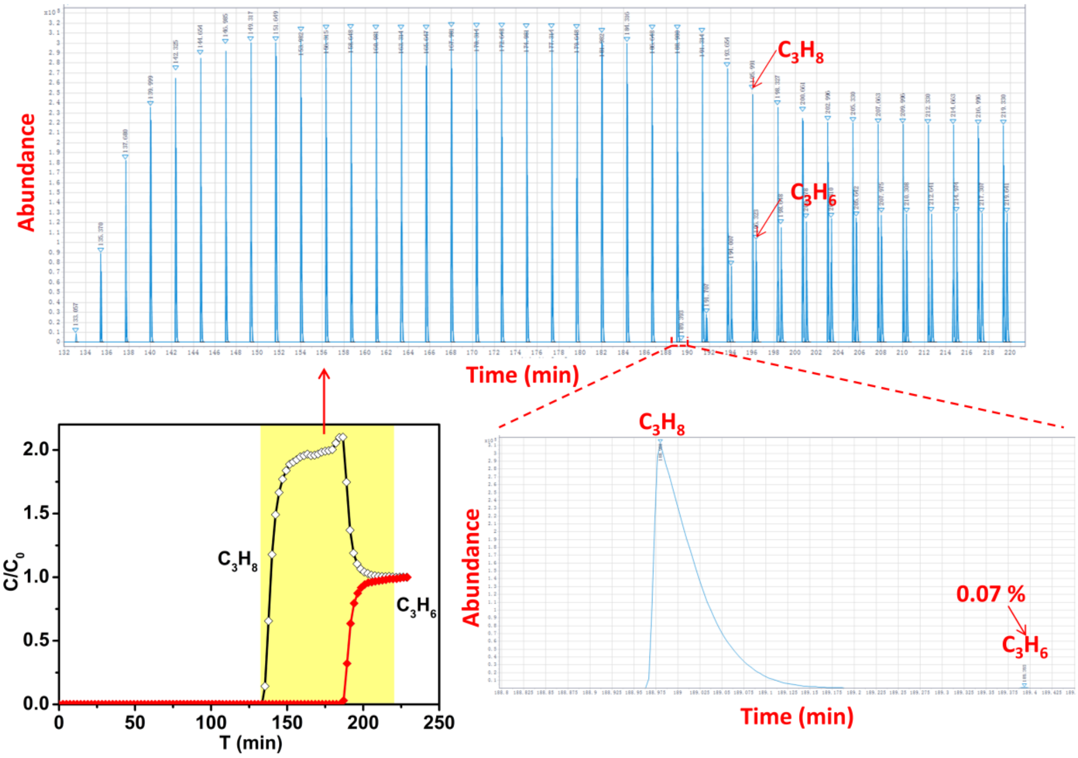

**Supplementary Figure 31.** Breakthrough curve and its corresponding GC chromatogram for XXU-3a with $C_3H_6/C_3H_8$ (50/50, 1 mL min$^{-1}$) as feed gas. The first $C_3H_6$ peak was observed at 189-min time point with an estimated concentration of 0.07%.

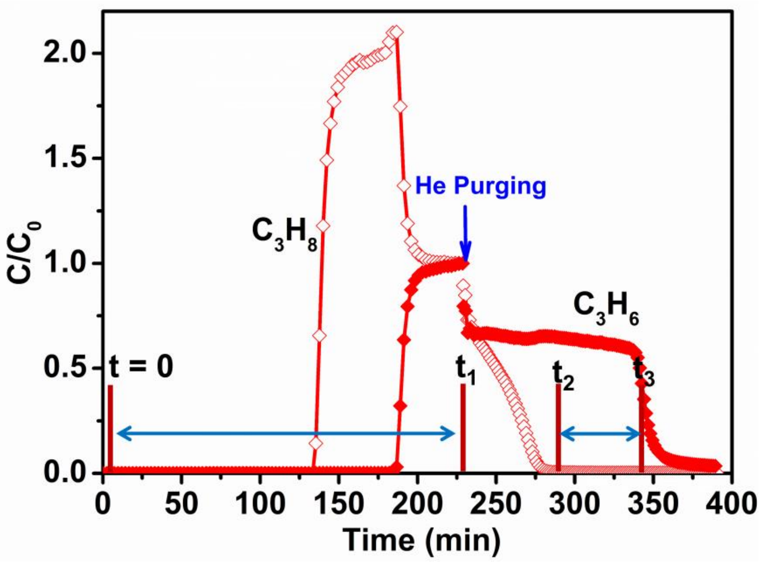

**Supplementary Figure 32.** The mixed gas input $q_{input}$ and $C_3H_6$ output $q_{output}$ were estimated by integrating the area from the time point $t_0$ to $t_1$ and $t_2$ to $t_3$ (breakthrough equilibrium point), respectively.

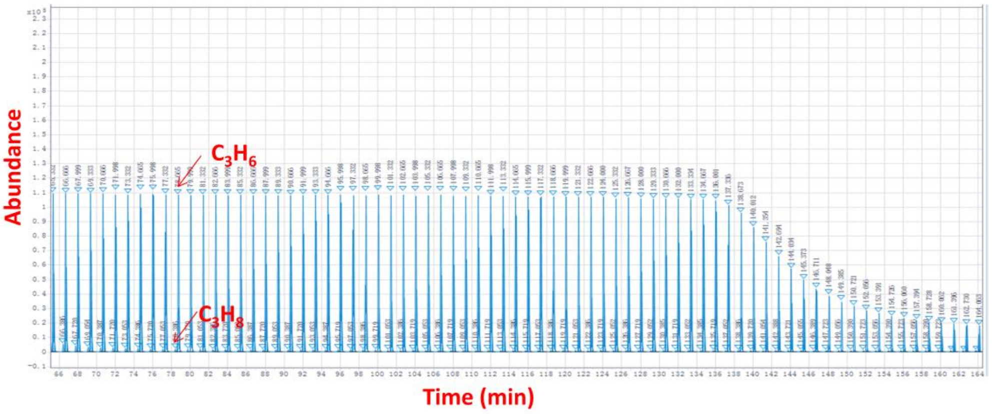

**Supplementary Figure 33.** GC chromatogram of the desorption from XXU-3a with helium sweeping (10 mL min$^{-1}$) at 303 K after the breakthrough of $C_3H_6$/$C_3H_8$ (50/50, 1.0 mL min$^{-1}$).

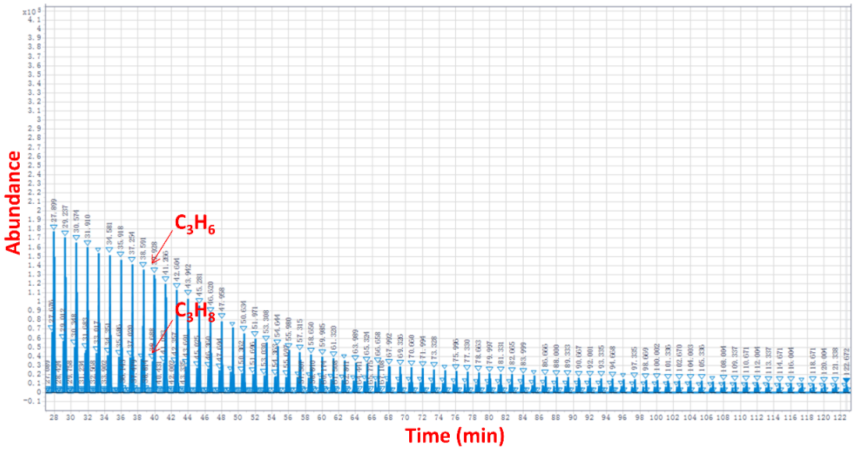

**Supplementary Figure 34.** GC chromatogram of the desorption from KAUST-7 with helium sweeping (10 mL min$^{-1}$) at 303 K after the breakthrough of $C_3H_6$/$C_3H_8$ (50/50, 1.0 mL min$^{-1}$).

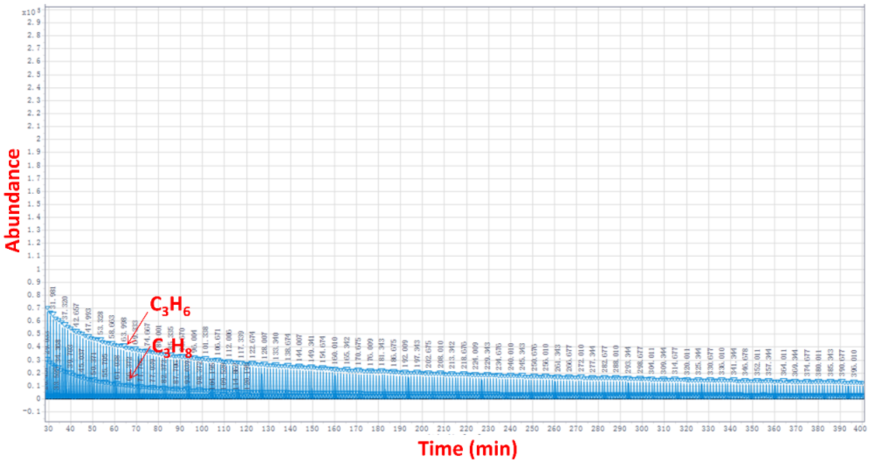

**Supplementary Figure 35.** GC chromatogram of the desorption from Y-abtc with helium sweeping He gas (10 mL min$^{-1}$) at 303 K after the breakthrough of $C_3H_6/C_3H_8$ (50/50, 1.0 mL min$^{-1}$).

The $C_3H_6$ purity (c) is defined by the peak area of $C_3H_6$, we calculated $C_3H_6$ purity according to the following equation:

$$\mathrm{c} = \frac{C_i(\mathrm{C_3H_6})}{C_i(\mathrm{C_3H_6}) + C_i(\mathrm{C_3H_8})}$$

where $C_{\mathrm{i}}(C_3H_6)$ and $C_{\mathrm{i}}(C_3H_6)$ represent the peak areas of component $C_3H_6$ and $C_3H_8$ in a single injection.

The $C_3H_6$ productivity (q) is defined by the breakthrough amount of $C_3H_6$, we calculated $C_3H_6$ productivity according to the following equation:

$$\mathrm{q} = \frac{\int_{t2}^{t3} f(t)\,\mathrm{d}t}{\mathrm{m}}$$

The $C_3H_6$ flow rate after breaking through was first determined by calibration curve of $C_3H_6$ flow rate *versus* its peak area on gas chromatogram (**Table S3** and **Figure S36**), the $C_3H_6$ productivity (q) was then calculated by integrating the $C_3H_6$ flow rate *f*(*t*) from *t*2 to *t*3 in which the $C_3H_6/C_3H_8$ ratio (peak area ratio) is over 99.5 %, m is the mass of XXU-3a used in the breakthrough experiment.

**Supplementary Table 3.** Peak area of $C_3H_6$ on gas chromatogram at different flowrates.

| **$C_3H_6$ flow rate (mL/min)** | **Peak area of $C_3H_6$ on gas chromatogram (5 runs for each flow rate)** | | | | |
|---|---|---|---|---|---|
| | 1 | 2 | 3 | 4 | 5 |
| **0.1** | 58942 | 60085 | 60115 | 60711 | 60422 |
| **0.2** | 73588 | 73544 | 73549 | 73536 | 73640 |
| **0.5** | 241123 | 240681 | 240749 | 241084 | 240869 |
| **0.8** | 360161 | 359271 | 358953 | 359185 | 359123 |
| **1** | 473615 | 471891 | 469637 | 467871 | 465114 |
| **1.2** | 519848 | 517785 | 516276 | 514993 | 514982 |
| **1.5** | 626476 | 625544 | 626171 | 625099 | 626163 |
| **1.8** | 686550 | 684589 | 682813 | 685151 | 684934 |
| **2** | 742834 | 746232 | 742676 | 744761 | 743772 |

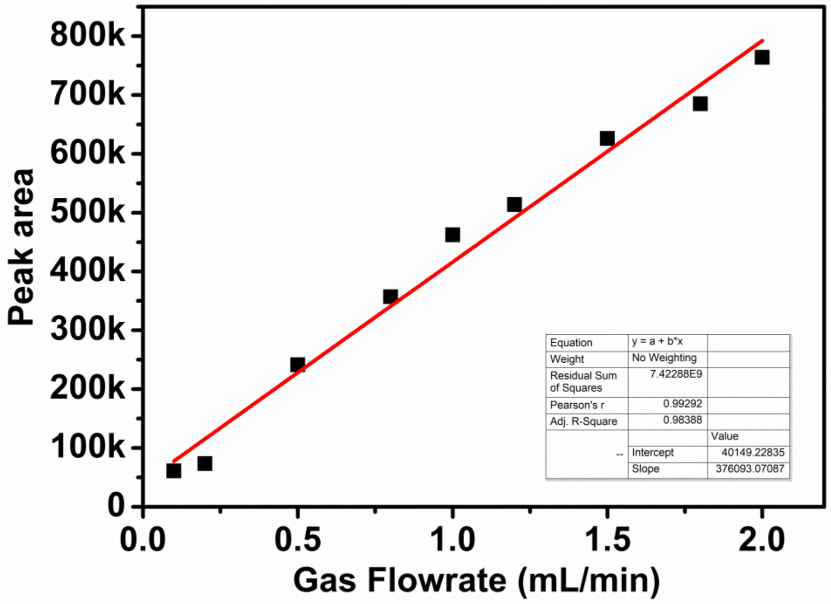

| Equation | y = a + b*x | |
|---|---|---|
| Weight | No Weighting | |
| Residual Sum of Squares | 7.42288E9 | |
| Pearson's r | 0.99292 | |
| Adj. R-Square | 0.98388 | |
| | | Value |
| -- | Intercept | 40149.22835 |
| | Slope | 376093.07087 |

**Supplementary Figure 36.** Calibration curve of $C_3H_6$ flow rate versus its peak area on the gas chromatogram.

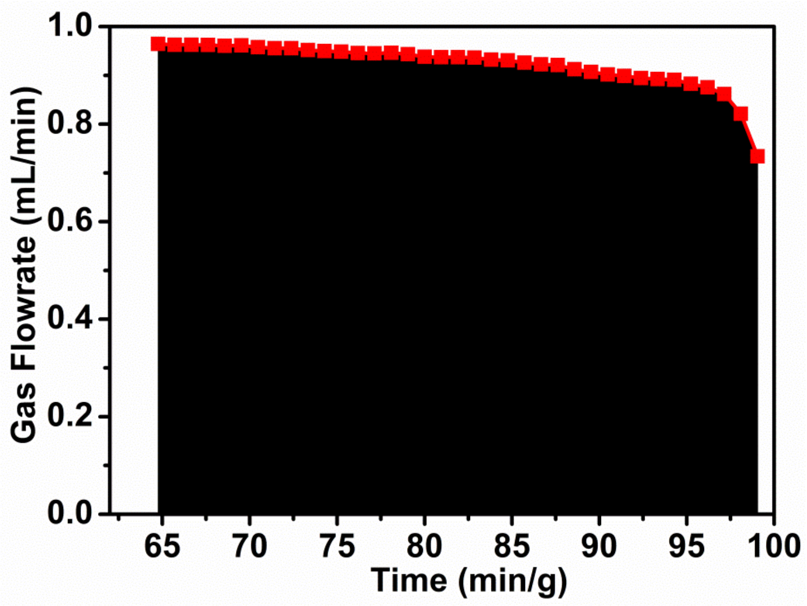

**Supplementary Figure 37.** $C_3H_6$ productivity for XXU-3a by integrating $C_3H_6$ flowrate *f*(*t*) from *t*2 to *t*3 in which the $C_3H_6/C_3H_8$ ratio (peak area ratio) is over 99.5 % after the breakthrough of an equimolar mixture of $C_3H_6/C_3H_8$ (1.0 mL min$^{-1}$).

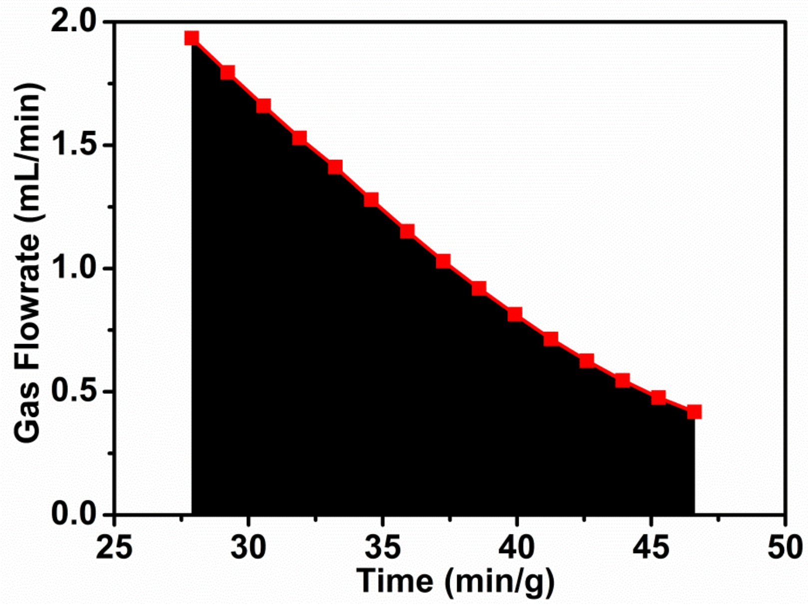

**Supplementary Figure 38.** $C_3H_6$ productivity for KAUST-7 by integrating $C_3H_6$ flowrate *f*(*t*) from *t*1 to *t*2 in which the $C_3H_6/C_3H_8$ ratio (peak area ratio) is over 90.0 % after the breakthrough of an equimolar mixture of $C_3H_6/C_3H_8$ (1.0 mL min$^{-1}$).

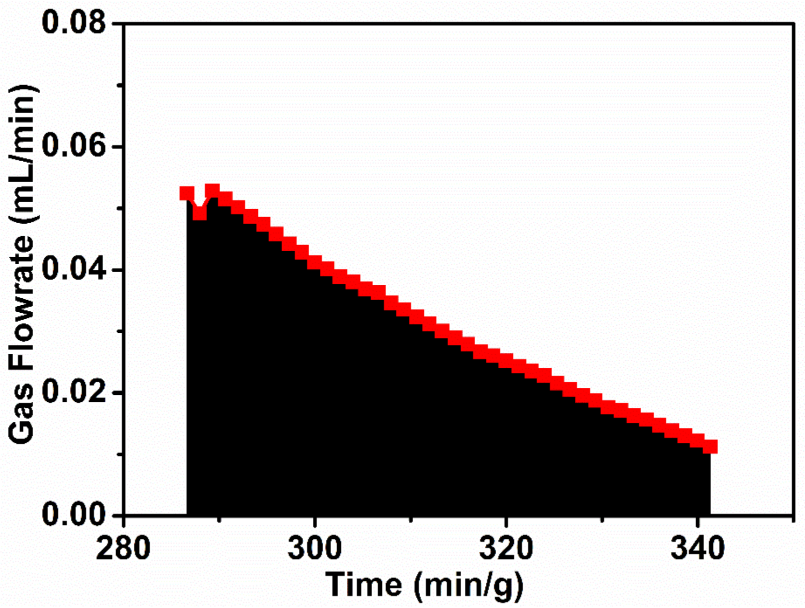

**Supplementary Figure 39.** $C_3H_6$ productivity for Y-abtc by integrating $C_3H_6$ flowrate $f(t)$ from $t2$ to $t3$ in which the $C_3H_6/C_3H_8$ ratio (peak area ratio) is over 90.0 % after the breakthrough of an equimolar mixture of $C_3H_6/C_3H_8$ (1.0 mL min$^{-1}$).

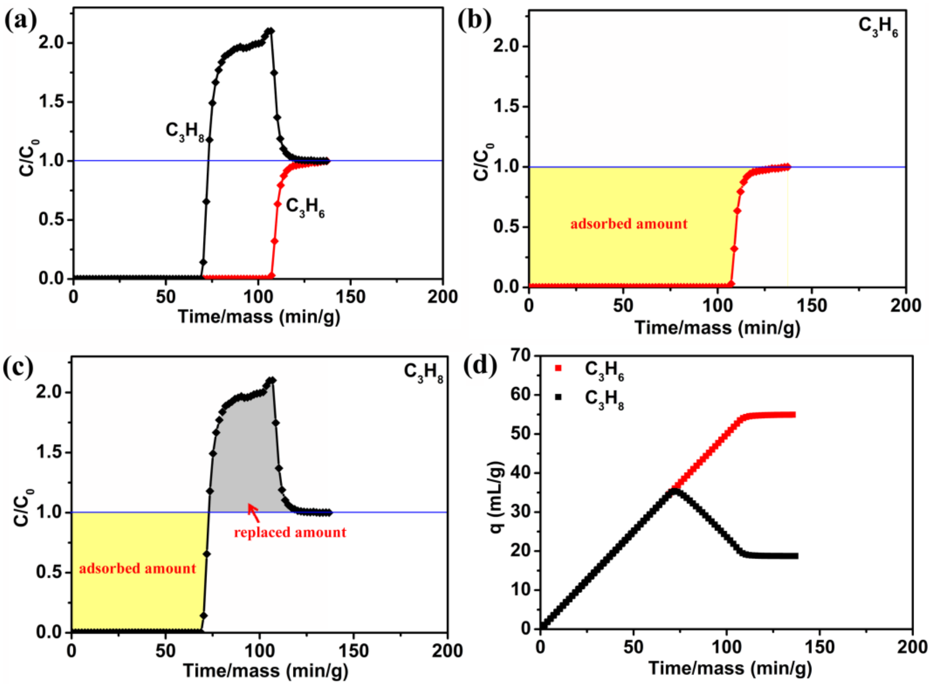

**Supplementary Figure 40.** (a) Breakthrough curves of an equimolar mixture of $C_3H_6/C_3H_8$ (1.0 mL min$^{-1}$) on XXU-3a. The adsorbed amount of (b) $C_3H_6$ and (c) $C_3H_8$ upon breakthrough equilibrium on XXU-3a, corresponding to the areas as highlighted on the breakthrough curves. (d) The adsorbed amount of $C_3H_6$ and $C_3H_8$ on XXU-3a as a function of time up to the time point of breakthrough equilibrium.

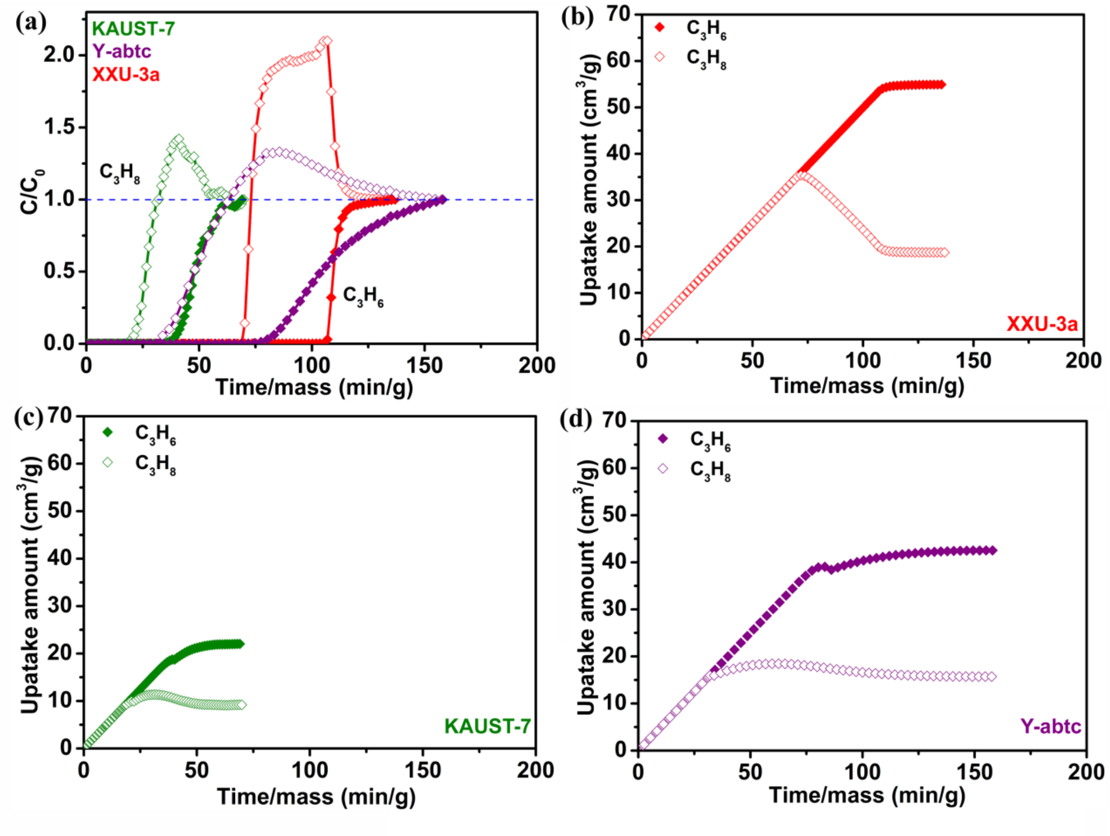

**Supplementary Figure 41.** Breakthrough curves of an equimolar mixture of $C_3H_6/C_3H_8$ (1.0 mL min$^{-1}$) on XXU-3a (1.4 g), KAUST-7 (1.2 g), and Y-abtc (0.9 g) at 303 K. The adsorbed amount of $C_3H_6$ and $C_3H_8$ as a function of time on XXU-3a, KAUST-7, and Y-abtc up to breakthrough equilibria. The x-axis is normalized to "time per gram adsorbents".

**Supplementary Table 4.** Summary of the adsorbed amount of $C_3H_6$ and $C_3H_8$ on XXU-3a, KAUST-7, and Y-abtc upon reaching breakthrough equilibria.

| **Materials** | **Uptake amount (cm$^3$/g)** | | **Ratios** |
|---|---|---|---|
| | **$C_3H_6$** | **$C_3H_8$** | $(\frac{q_{C3H6}}{q_{C3H8}})$ |
| **XXU-3a** | 54.9 | 18.7 | 2.9 |
| **KAUST-7** | 22.0 | 9.2 | 2.3 |
| **Y-abtc** | 42.5 | 15.7 | 2.7 |

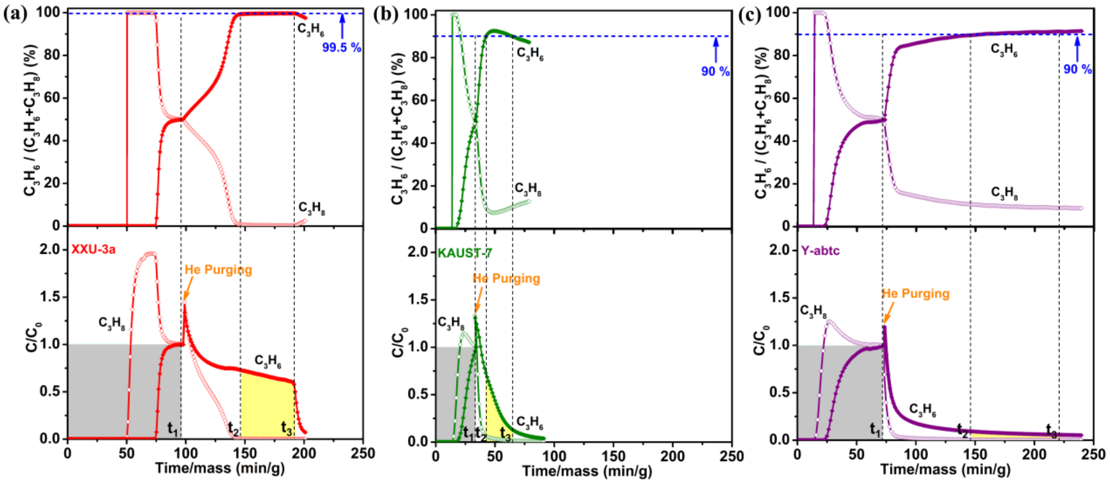

**Supplementary Figure 42.** Breakthrough curves of an equimolar mixture of $C_3H_6$/$C_3H_8$ (2.0 mL min$^{-1}$) on XXU-3a (1.4 g), KAUST-7 (1.2 g), and Y-abtc (0.9 g) followed by desorption curves under helium gas (10.0 mL min$^{-1}$) sweeping at 303 K. $C_3H_8$ (open diamonds), $C_3H_6$ (solid diamonds). ($C_0$ = 2.0 mL min$^{-1}$ before breakthrough equilibrium, and $C_0$ = 1.0 mL min$^{-1}$ upon He purging). The x-axis is normalized to "time per gram adsorbents".

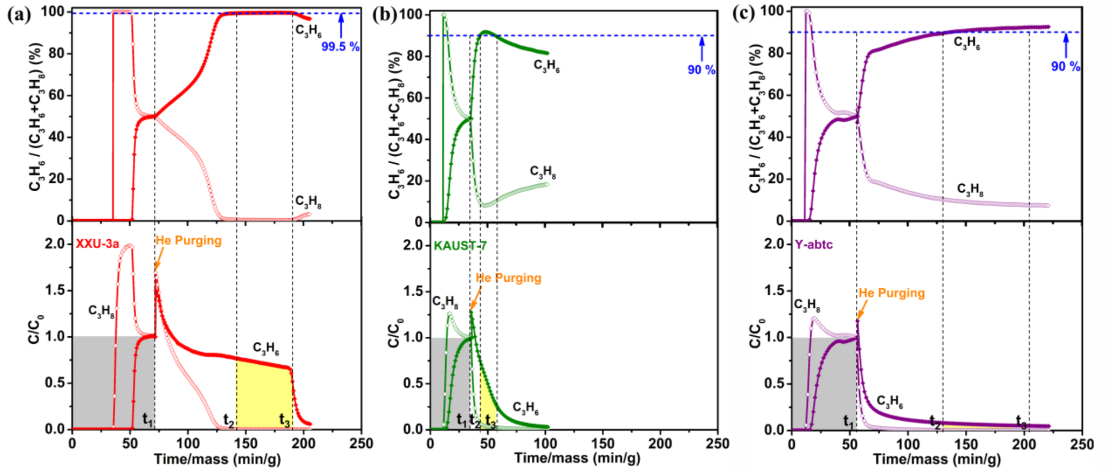

**Supplementary Figure 43.** Breakthrough curves of an equimolar mixture of $C_3H_6$/$C_3H_8$ (3.0 mL min$^{-1}$) on XXU-3a (1.4 g), KAUST-7 (1.2 g), and Y-abtc (0.9 g) followed by desorption curves under helium gas (10.0 mL min$^{-1}$) sweeping at 303 K. $C_3H_8$ (open diamonds), $C_3H_6$ (solid diamonds). ($C_0$ = 3.0 mL min$^{-1}$ before breakthrough equilibrium, and $C_0$ = 1.0 mL min$^{-1}$ upon He purging). The x-axis is normalized to "time per gram adsorbents".

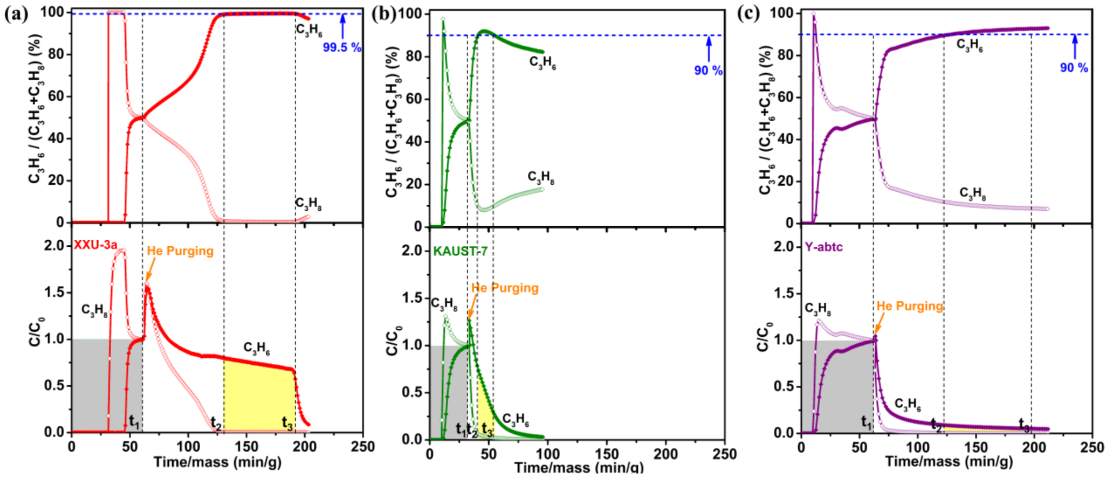

**Supplementary Figure 44.** Breakthrough curves of an equimolar mixture of $C_3H_6$/$C_3H_8$ (4.0 mL min$^{-1}$) on XXU-3a (1.4 g), KAUST-7 (1.2 g), and Y-abtc (0.9 g) followed by desorption curves under helium gas (10.0 mL min$^{-1}$) sweeping at 303 K. $C_3H_8$ (open diamonds), $C_3H_6$ (solid diamonds). ($C_0$ = 4.0 mL min$^{-1}$ before breakthrough equilibrium, and $C_0$ = 1.0 mL min$^{-1}$ upon He purging). The x-axis is normalized to "time per gram adsorbents".

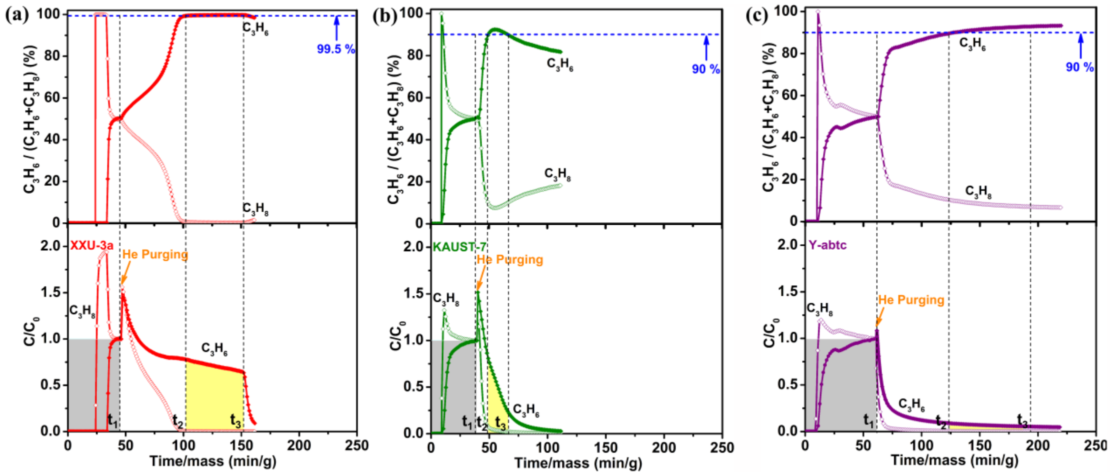

**Supplementary Figure 45.** Breakthrough curves of an equimolar mixture of $C_3H_6$/$C_3H_8$ (5.0 mL min$^{-1}$) on XXU-3a (1.4 g), KAUST-7 (1.2 g), and Y-abtc (0.9 g) followed by desorption curves under helium gas (10.0 mL min$^{-1}$) sweeping at 303 K. $C_3H_8$ (open diamonds), $C_3H_6$ (solid diamonds). ($C_0$ = 5.0 mL min$^{-1}$ before breakthrough equilibrium, and $C_0$ = 1.0 mL min$^{-1}$ upon He purging). The x-axis is normalized to "time per gram adsorbents".

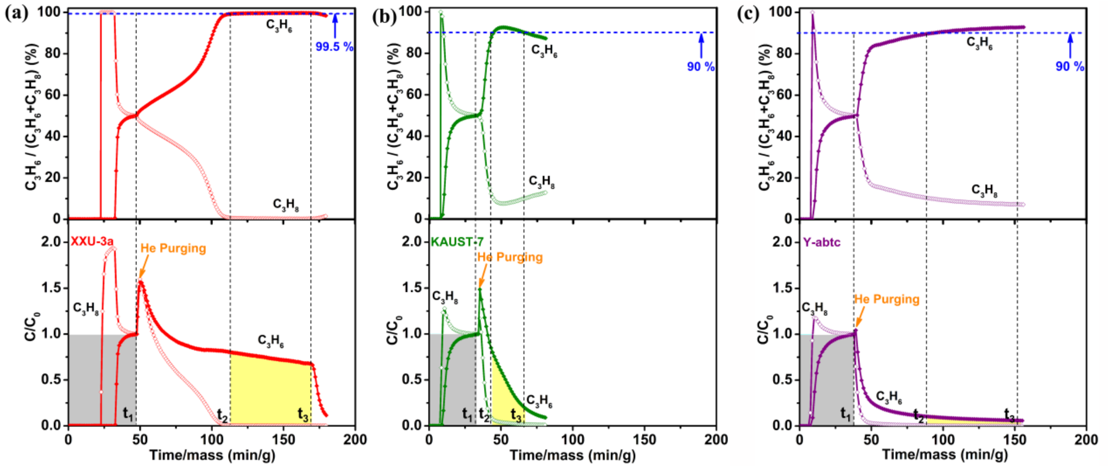

**Supplementary Figure 46.** Breakthrough curves of an equimolar mixture of $C_3H_6$/$C_3H_8$ (6.0 mL min$^{-1}$) on XXU-3a (1.4 g), KAUST-7 (1.2 g), and Y-abtc (0.9 g) followed by desorption curves under helium gas (10.0 mL min$^{-1}$) sweeping at 303 K. $C_3H_8$ (open diamonds), $C_3H_6$ (solid diamonds). ($C_0$ = 6.0 mL min$^{-1}$ before breakthrough equilibrium, and $C_0$ = 1.0 mL min$^{-1}$ upon He purging). The x-axis is normalized to "time per gram adsorbents".

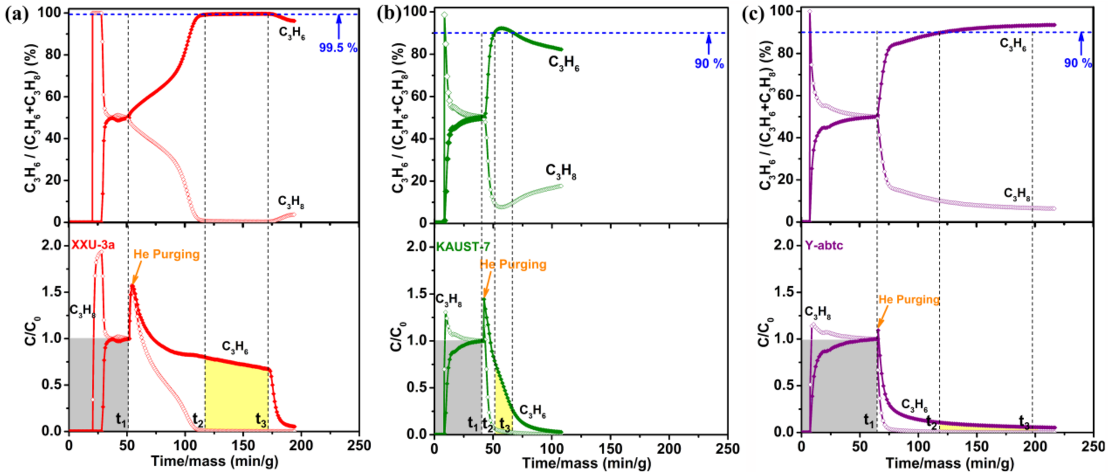

**Supplementary Figure 47.** Breakthrough curves of an equimolar mixture of $C_3H_6$/$C_3H_8$ (7.0 mL min$^{-1}$) on XXU-3a (1.4 g), KAUST-7 (1.2 g), and Y-abtc (0.9 g) followed by desorption curves under helium gas (10.0 mL min$^{-1}$) sweeping at 303 K. $C_3H_8$ (open diamonds), $C_3H_6$ (solid diamonds). ($C_0$ = 7.0 mL min$^{-1}$ before breakthrough equilibrium, and $C_0$ = 1.0 mL min$^{-1}$ upon He purging). The x-axis is normalized to "time per gram adsorbents".

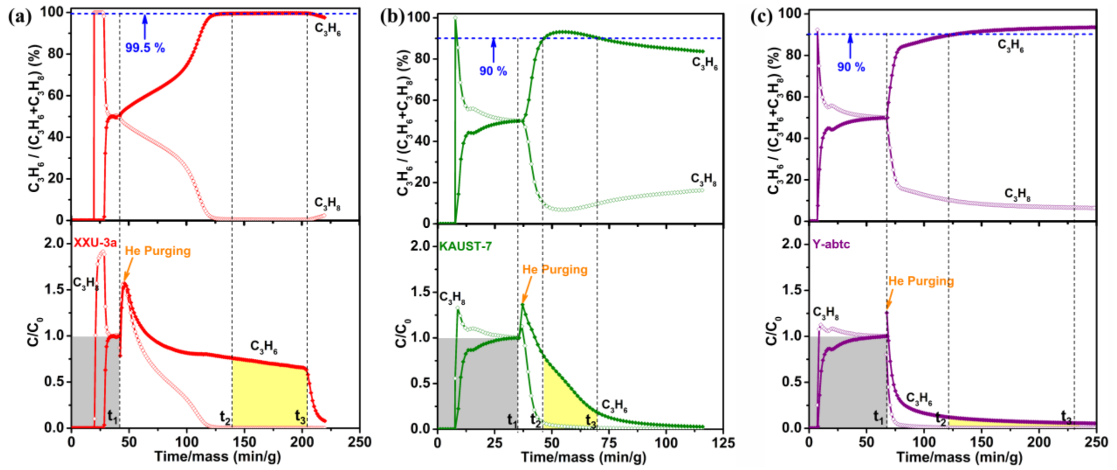

**Supplementary Figure 48.** Breakthrough curves of an equimolar mixture of $C_3H_6/C_3H_8$ (8.0 mL min$^{-1}$) on XXU-3a (1.4 g), KAUST-7 (1.2 g), and Y-abtc (0.9 g) followed by desorption curves under helium gas (10.0 mL min$^{-1}$) sweeping at 303 K. $C_3H_8$ (open diamonds), $C_3H_6$ (solid diamonds). ($C_0$ = 8.0 mL min$^{-1}$ before breakthrough equilibrium, and $C_0$ = 1.0 mL min$^{-1}$ upon He purging). The x-axis is normalized to "time per gram adsorbents".

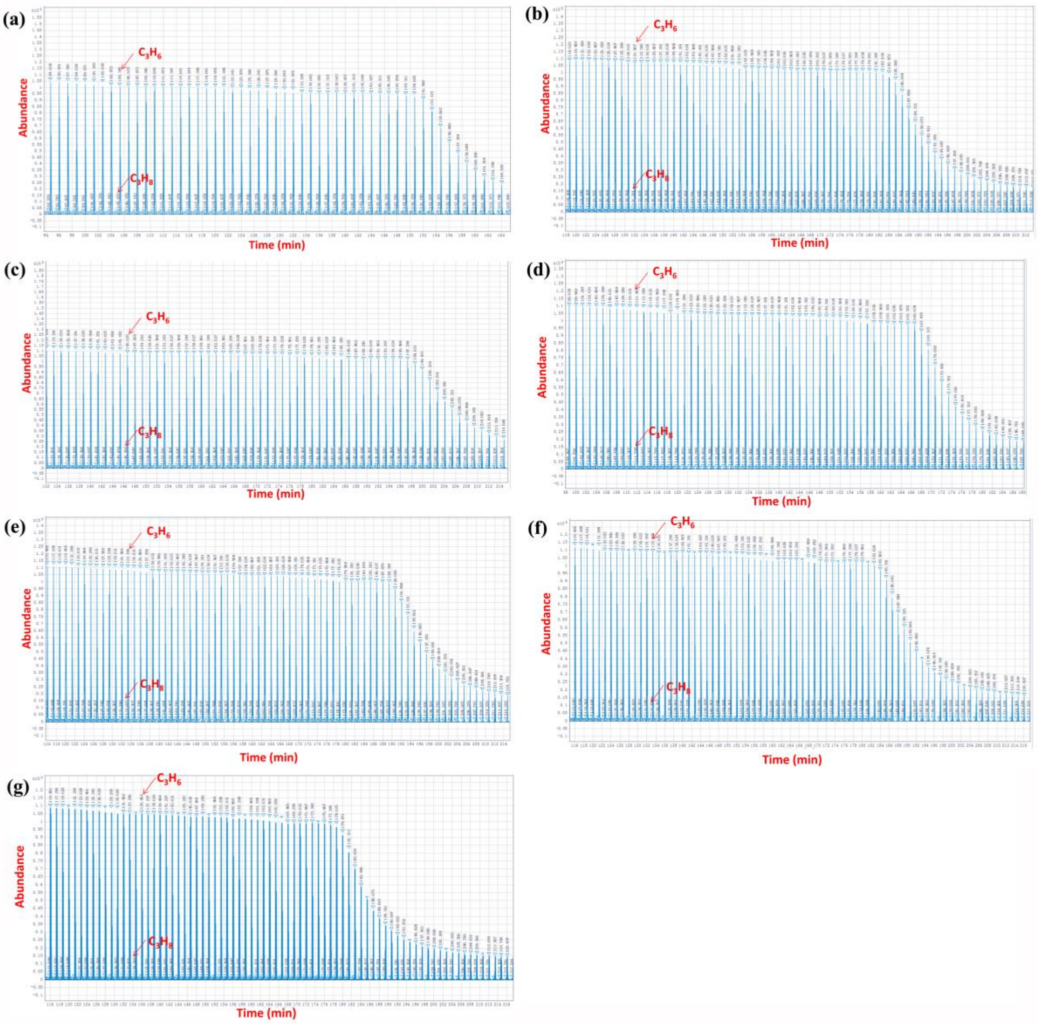

**Supplementary Figure 49.** GC chromatogram of the desorption from XXU-3a with helium sweeping (10 mL min$^{-1}$) at 303 K after the breakthrough of an equimolar $C_3H_6/C_3H_8$ mixture at a flowrate of (a) 2.0 mL min$^{-1}$, (b) 3.0 mL min$^{-1}$, (c) 4.0 mL min$^{-1}$ (d) 5.0 mL min$^{-1}$, (e) 6.0 mL min$^{-1}$, (f) 7.0 mL min$^{-1}$ and (g) 8.0 mL min$^{-1}$.

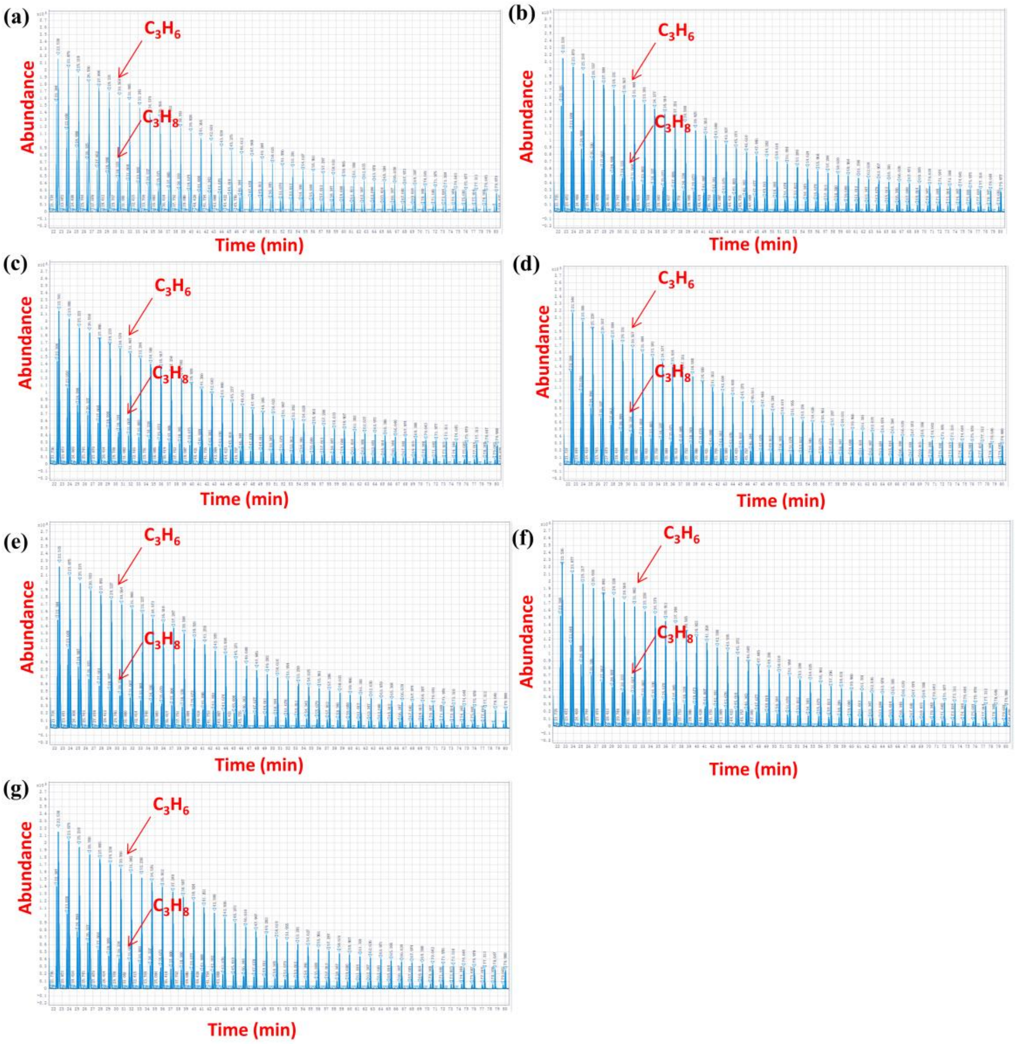

**Supplementary Figure 50.** GC chromatogram of the desorption from KAUST-7 with helium sweeping (10 mL min$^{-1}$) at 303 K after the breakthrough of an equimolar $C_3H_6/C_3H_8$ mixture at a flowrate of (a) 2.0 mL min$^{-1}$, (b) 3.0 mL min$^{-1}$, (c) 4.0 mL min$^{-1}$ (d) 5.0 mL min$^{-1}$, (e) 6.0 mL min$^{-1}$, (f) 7.0 mL min$^{-1}$ and (g) 8.0 mL min$^{-1}$.

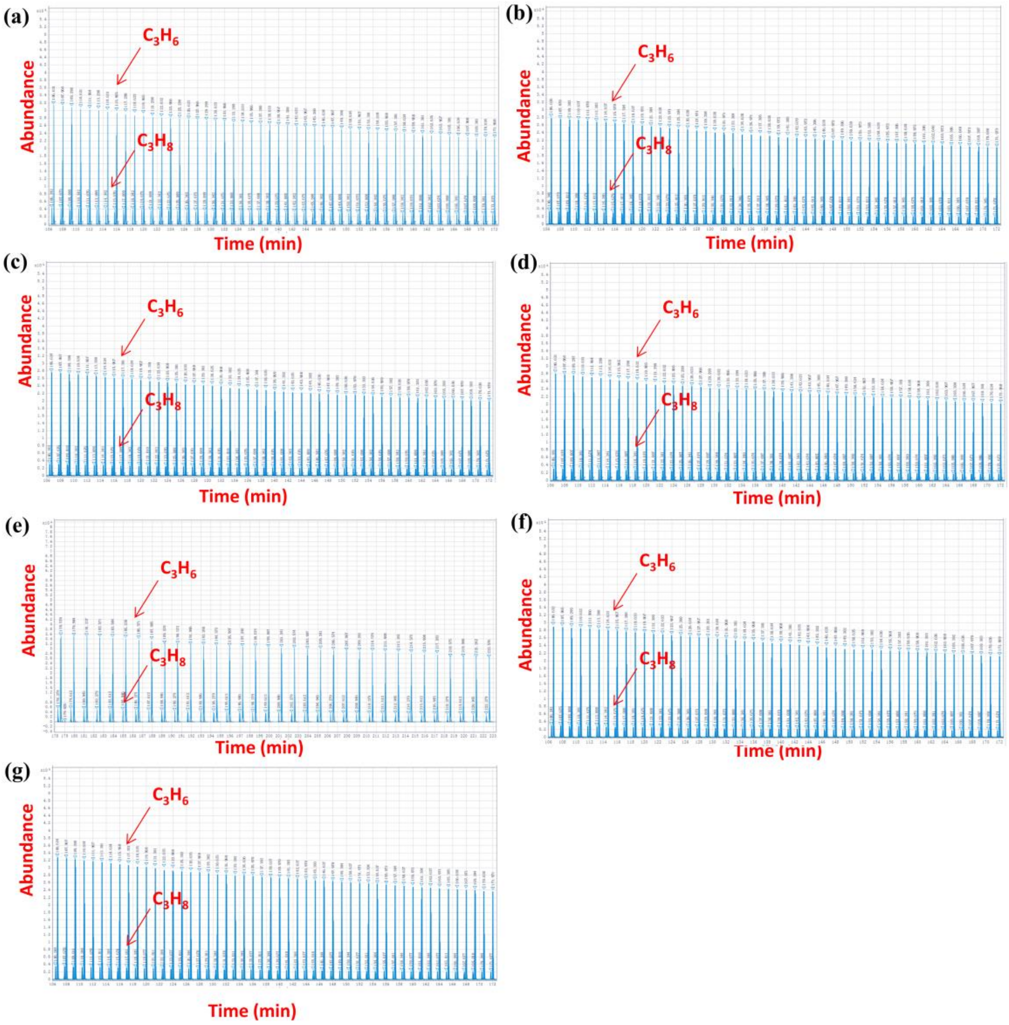

**Supplementary Figure 51.** GC chromatogram of the desorption from Y-abtc with helium sweeping (10 mL min$^{-1}$) at 303 K after the breakthrough of an equimolar $C_3H_6$/$C_3H_8$ mixture at a flowrate of (a) 2.0 mL min$^{-1}$, (b) 3.0 mL min$^{-1}$, (c) 4.0 mL min$^{-1}$ (d) 5.0 mL min$^{-1}$, (e) 6.0 mL min$^{-1}$, (f) 7.0 mL min$^{-1}$ and (g) 8.0 mL min$^{-1}$.

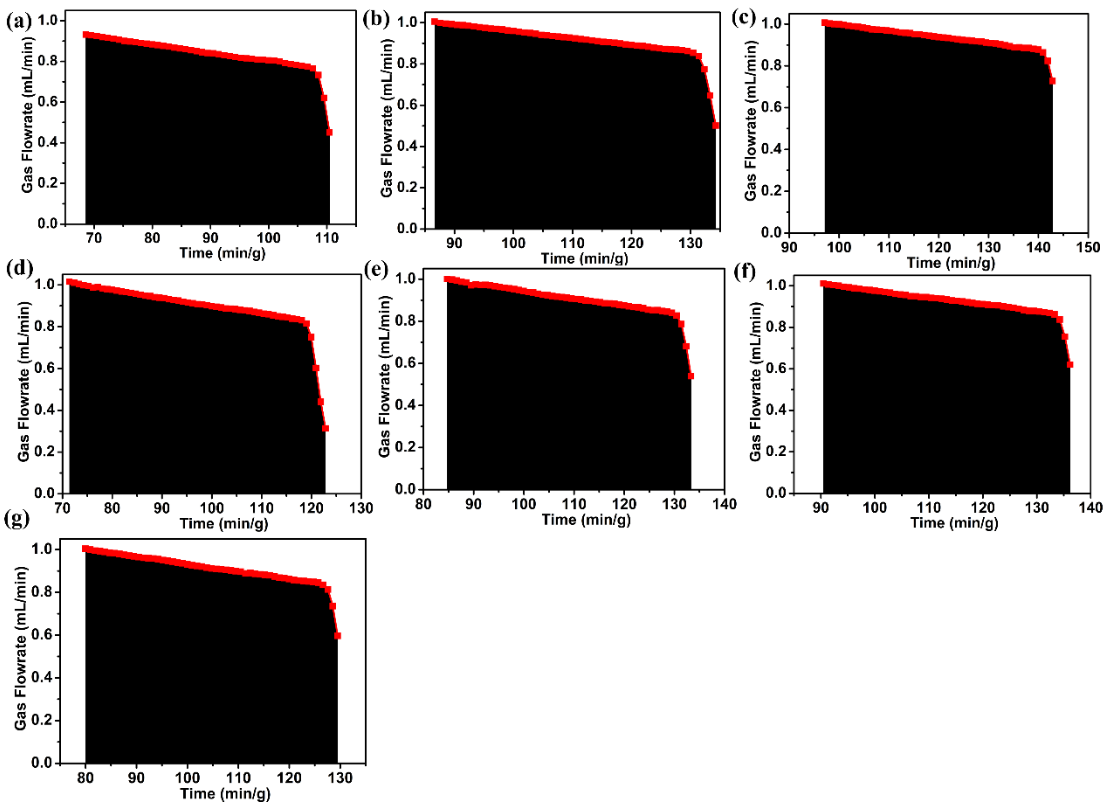

**Supplementary Figure 52.** $C_3H_6$ productivity for XXU-3a by integrating $C_3H_6$ flowrate *f*(*t*) from *t*2 to *t*3 in which the $C_3H_6/C_3H_8$ ratio (peak area ratio) is over 99.5 % after the breakthrough of an equimolar mixture of $C_3H_6/C_3H_8$ at a flowrate of (a) 2.0 mL min$^{-1}$, (b) 3.0 mL min$^{-1}$, (c) 4.0 mL min$^{-1}$ (d) 5.0 mL min$^{-1}$, (e) 6.0 mL min$^{-1}$, (f) 7.0 mL min$^{-1}$ and (g) 8.0 mL min$^{-1}$.

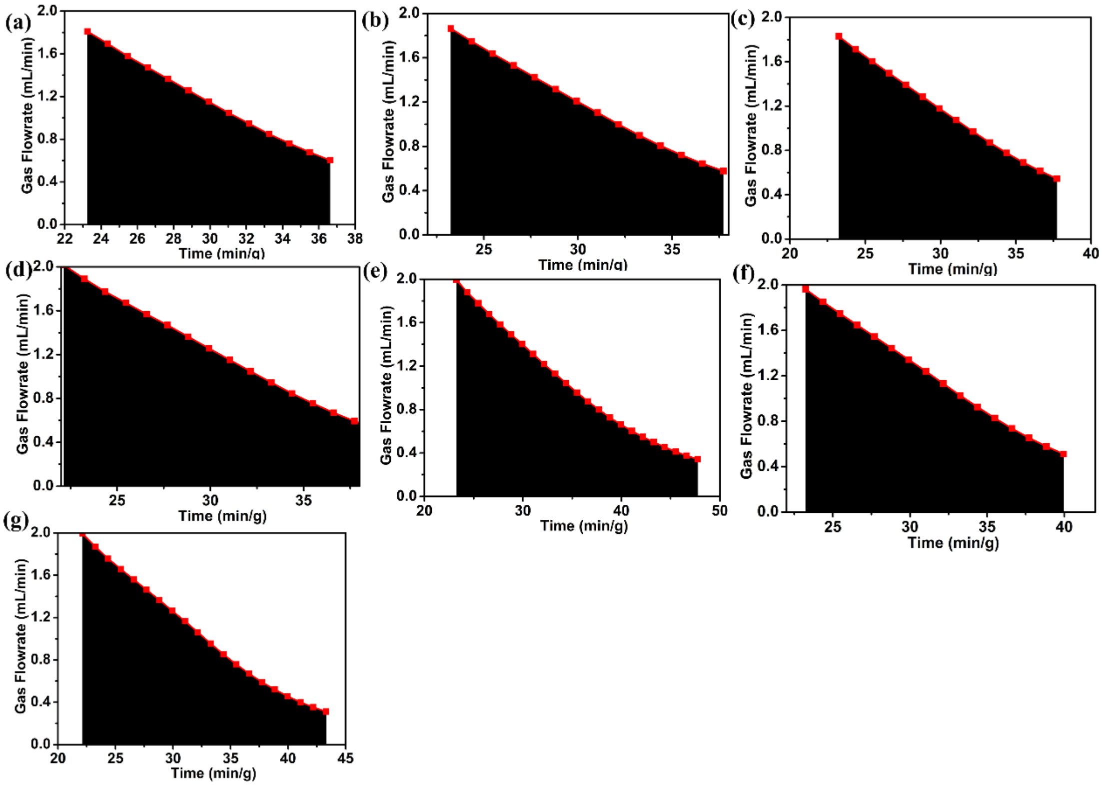

**Supplementary Figure 53.** $C_3H_6$ productivity for KAUST-7 by integrating $C_3H_6$ flowrate *f*(*t*) from *t*2 to *t*3 in which the $C_3H_6/C_3H_8$ ratio (peak area ratio) is over 90 % after the breakthrough of an equimolar mixture of $C_3H_6/C_3H_8$ at a flowrate of (a) 2.0 mL min$^{-1}$, (b) 3.0 mL min$^{-1}$, (c) 4.0 mL min$^{-1}$ (d) 5.0 mL min$^{-1}$, (e) 6.0 mL min$^{-1}$, (f) 7.0 mL min$^{-1}$ and (g) 8.0 mL min$^{-1}$.

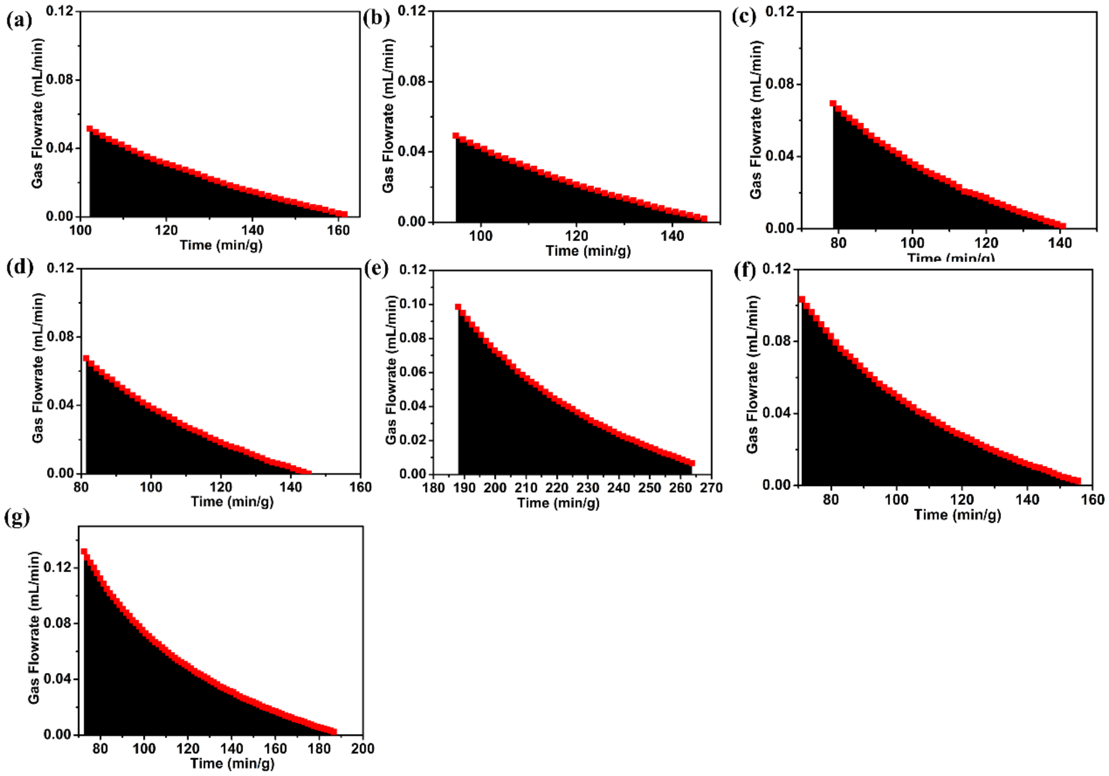

**Supplementary Figure 54.** $C_3H_6$ productivity for Y-abtc by integrating $C_3H_6$ flowrate *f*(*t*) from *t*2 to *t*3 in which the $C_3H_6/C_3H_8$ ratio (peak area ratio) is over 90 % after the breakthrough of an equimolar mixture of $C_3H_6/C_3H_8$ at a flowrate of (a) 2.0 mL $min^{-1}$, (b) 3.0 mL $min^{-1}$, (c) 4.0 mL $min^{-1}$ (d) 5.0 mL $min^{-1}$, (e) 6.0 mL $min^{-1}$, (f) 7.0 mL $min^{-1}$ and (g) 8.0 mL $min^{-1}$.

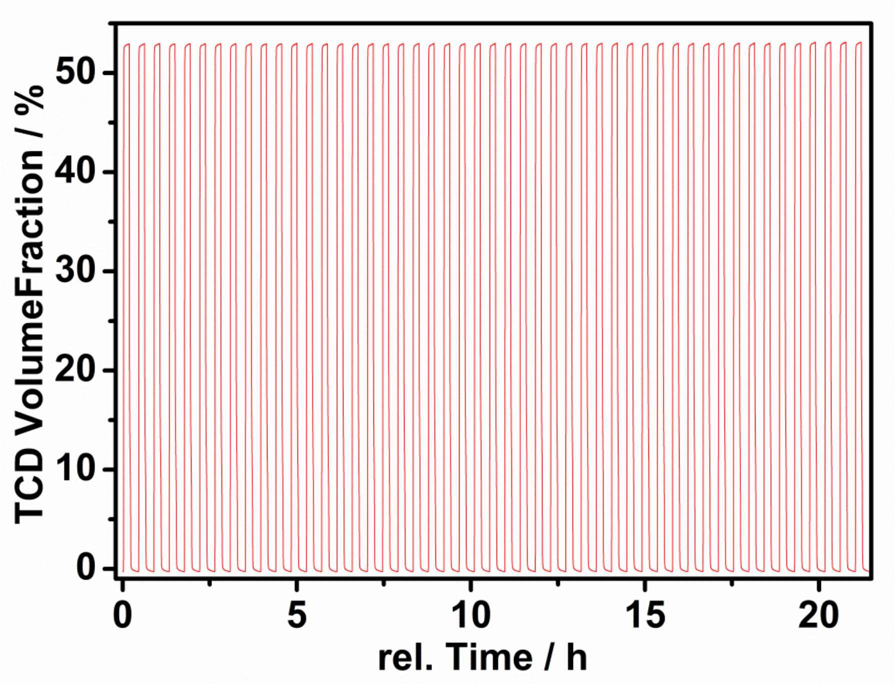

**Supplementary Figure 55.** Fifty continuous breakthrough experiments of pure $C_3H_6$ on XXU-3a at 303 K. Desorption was carried out by helium sweeping at 303 K between cycles, no obvious loss of uptake capacity was observed.

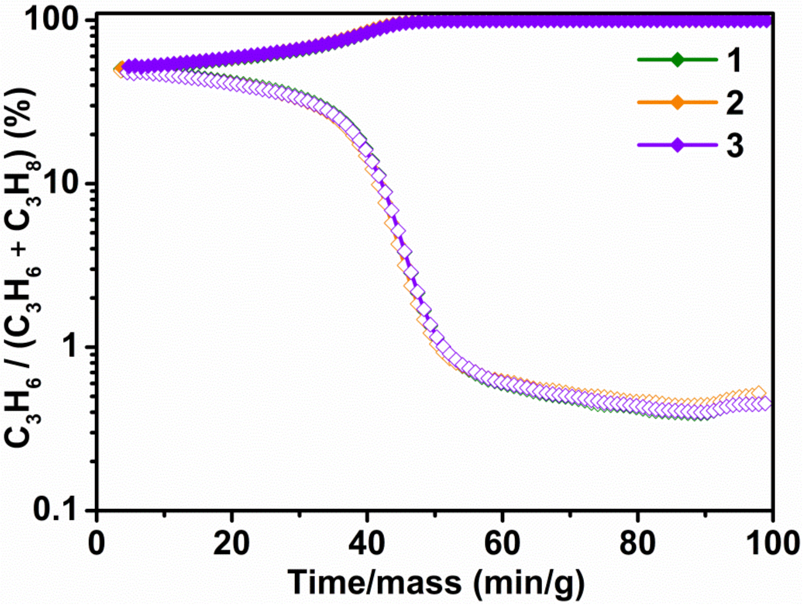

**Supplementary Figure 56.** Three desorption curves of XXU-3a under helium gas sweeping (10.0 mL min$^{-1}$) at 303 K after breakthroughs for an equimolar $C_3H_6/C_3H_8$ mixture at a flowrate of 1.0 mL min$^{-1}$.

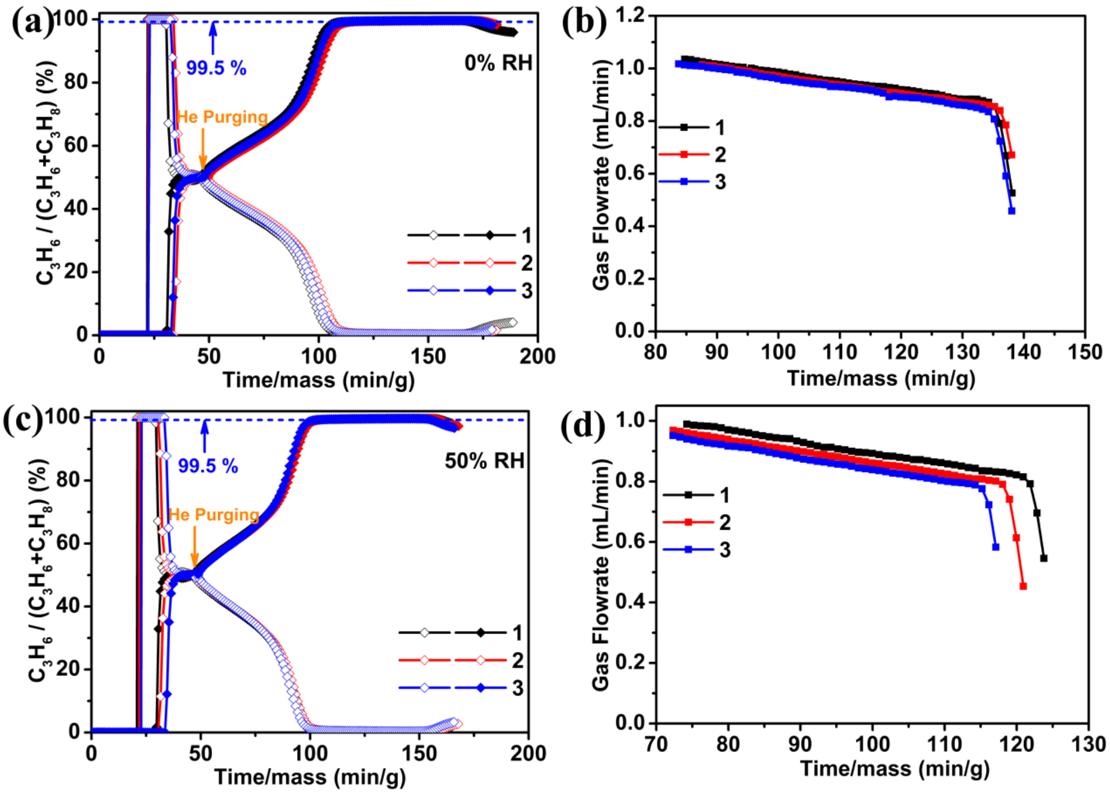

**Supplementary Figure 57.** Three breakthrough curves and its corresponding $C_3H_6$ productivity for an equimolar mixture of $C_3H_6$/$C_3H_8$ at a flowrate of 6.0 mL min$^{-1}$ on XXU-3a under dry (a,b) and humid (c,d) conditions (50 % RH), followed by desorption curves under helium gas sweeping (10.0 mL min$^{-1}$) at 303 K. $C_3H_8$ (open diamonds), $C_3H_6$ (solid diamonds).

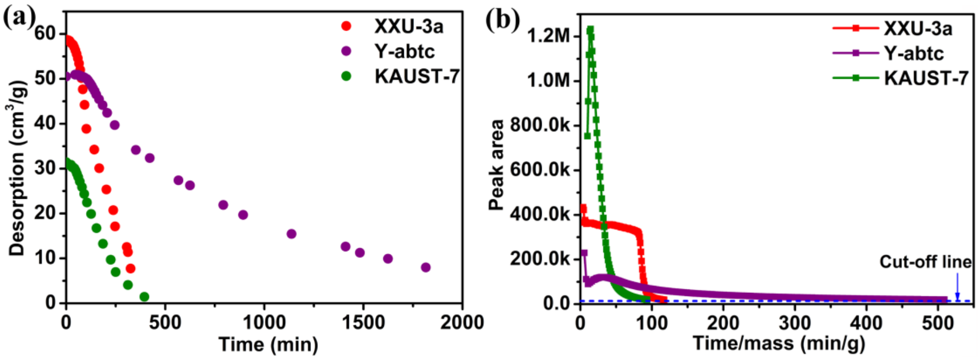

**Supplementary Figure 58.** $C_3H_6$ kinetic desorption profiles for XXU-3a, Y-abtc, and KAUST-7 at 303 K collected on Micromeritics ASAP 2020 Plus. GC chromatogram of $C_3H_6$ peak areas in the desorption process of the breakthrough experiments on XXU-3a, Y-abtc, and KAUST-7. The x-axis is normalized to "time per gram adsorbents".

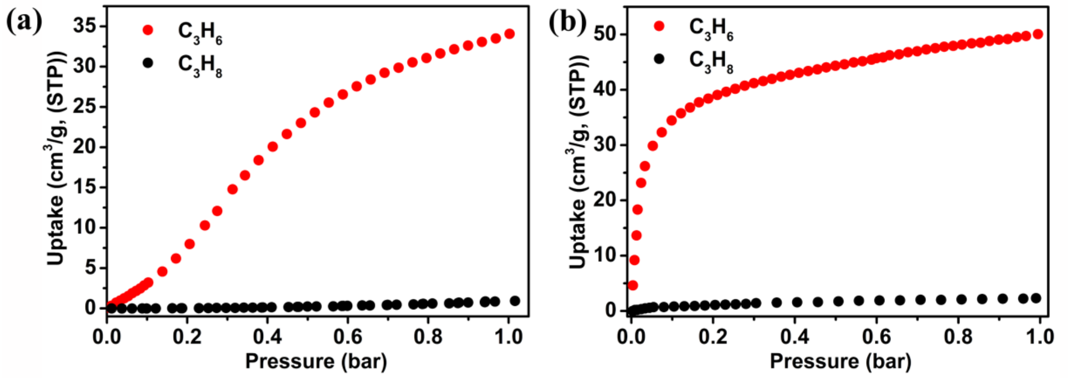

**Supplementary Figure 59.** (a) $C_3H_6$ and $C_3H_8$ single-component adsorption isotherms of KAUST-7 (synthesized according to the reported procedure[7]) at 303 K. (b) $C_3H_6$ and $C_3H_8$ single-component adsorption isotherms of Y-abtc (synthesized according to the reported procedure[8]) at 303 K.

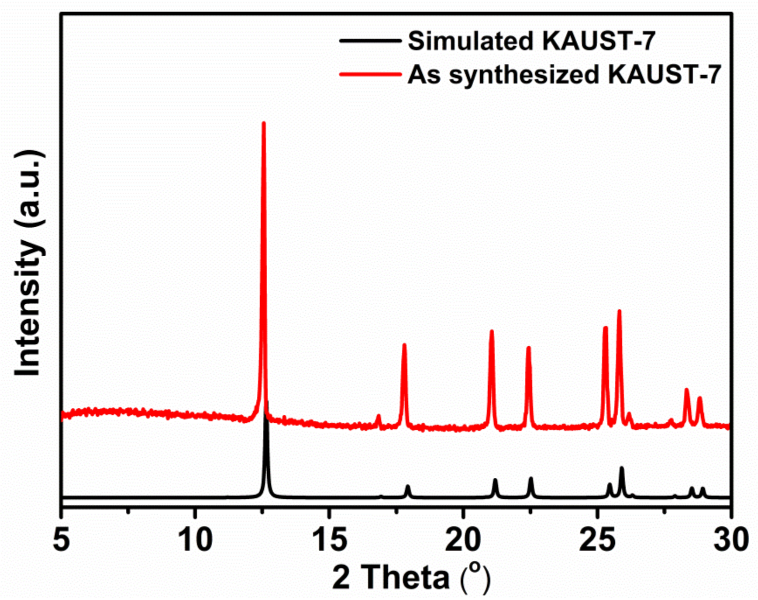

**Supplementary Figure 60.** PXRD patterns of the simulated (black) and as-synthesized KAUST-7.

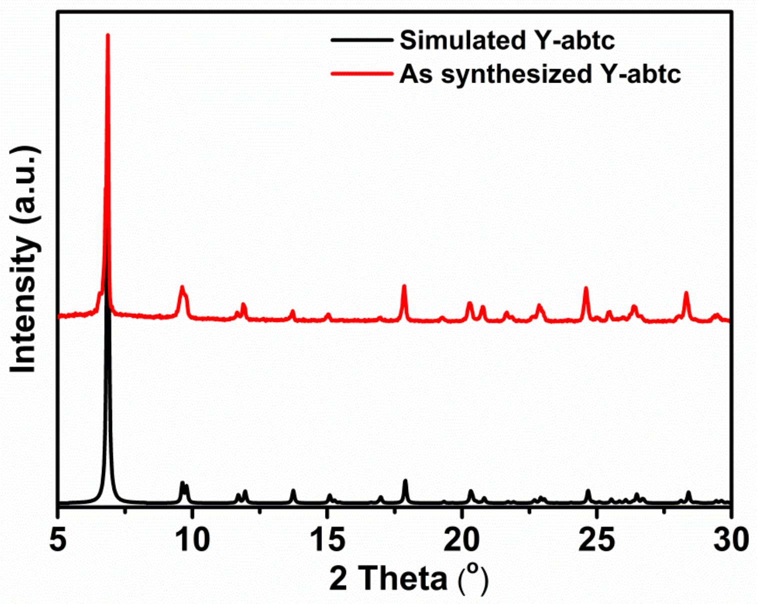

**Supplementary Figure 61.** PXRD patterns of the simulated (black) and as-synthesized Y-abtc.

**Supplementary Table 5.** Summary of the adsorption capacity of $C_3H_6$ and $C_3H_8$, as well as $C_3H_6/C_3H_8$ (50/50) selectivity in some selected MOFs (reorganized from refs. 6-16).

| **MOFs** | **$C_3H_6$ (cm$^3$ g$^{-1}$, STP)** | **$C_3H_8$ (cm$^3$ g$^{-1}$, STP)** | **$C_3H_6/C_3H_8$ (1/1) selectivity** | **$Q_{st}$ of $C_3H_6$ (kJ mol$^{-1}$)** | **Condition** | **Ref** |
|---|---|---|---|---|---|---|
| KAUST-7 | 32 | 1.2 | / | 57.4 | 298 K, 100 kPa | 7 |
| ITQ-12 | ~29.1 | ~16.8 | 15 | / | 303 K, 100 kPa | 9 |
| $Fe_2$(dobdc) | ~159.0 | ~136.6 | 14.7 | 44 | 298 K, 100 kPa | 10 |
| $Fe_2$(m-dobdc) | >156.0 | ~134.4 | >55 | 65 | 298 K, 100 kPa | 11 |
| $Cu_2(BTC)_3$ | ~179.2 | ~152.3 | / | 41.8 | 323 K, 100 kPa | 12 |
| ZIF-7 | ~56 | ~51.5 | / | / | 298 K, 100 kPa | 13 |
| CPL-1 | ~40.8 | ~6.5 | 2.08 | / | 273 K, 100 kPa | 14 |
| NJU-Bai8 | 60.5 | 1.4 | 4.6 | / | 298 K, 20 kPa | 15 |
| Y-abtc | ~44.8 | 2.6 | / | ~50 | 298 K, 100 kPa | 8 |
| NKU-FlexMOF-1 | ~70 | ~60 | / | 61.6 | 298 K, 100 kPa | 16 |
| ELM-14 | 33.0 | 30.5 | 204[a] | / | 298 K, 100 kPa | 17 |
| **Co-gallate** | 39.8 | 3.1 | 330 | 41 | 298 K, 100 kPa | 18 |
| XXU-3a | 58.6 | 48.0 | 513 | 33 | 303 K, 100 kPa | |

[a] Kinetic selectivity

## References

1. Dincă, M.; Dailly, A.; Liu, Y.; Brown, C. M.; Neumann, D. A.; Long, J. R., Hydrogen Storage in a M icroporous Metal-Organic Framework with Exposed $Mn^{2+}$ Coordination Sites. *J. Am. Chem. Soc.* **128**, 16876-16883 (2006).
2. Myers, A. L.; Prausnitz, J.M. Thermodynamics of mixed-gas adsorption. *AIChE J.* **11**, 121-127 (1965).
3. Webster, C. E., Drago, R. S. & Zerner, M. C. Molecular Dimensions for Adsorptives. *J. Am. Chem. Soc.* **120**, 5509-5516 (1998).
4. Kärger, J., Ruthven, D. M., Theodorou, D. N. Diffusion in Nanoporous Materials (Wiley, 2012).
5. Grimme, S. Semiempirical GGA-type density functional constructed with a long-range dispersion correction. *J. Chem. Phys.* 27, 1787-1799 (2006).
6. Weigend, F. & Ahlrichs, R. Balanced basis sets of split valence, triple zeta valence and quadruple zeta valence quality for H to Rn: design and assessment of accuracy. *Phys. Chem. Chem. Phys.* 7, 3297-3305 (2005).
6. J. Liu, J. Tian, P. K. Thallapally, B. P. McGrail, Selective $CO_2$ Capture from Flue Gas Using Metal-Organic Frameworks-A Fixed Bed Study. *J. Phys. Chem. C* **116**, 9575-9581 (2012).
7. Cadiau, A., Adil, K., Bhatt, P. M., Belmabkhout, Y., Eddaoudi, M. A metal-organic framework-based splitter for separating propylene from propane, *Science* **353**, 137-140 (2016).
8. Li, J. et al. Tailor-Made Microporous Metal-Organic Frameworks for the Full Separation of Propane from Propylene Through Selective Size Exclusion. *Adv. Mater.* **30**, 1805088 (2018).
9. Gutiérrez-Sevillano, J. J., Dubbeldam, D., Rey, F., Valencia, S., Palomino, M., MartínCalvo, A., Calero, S. A. Analysis of the ITQ-12 zeolite performance in propane-propylene separations using a combination of experiments and molecular simulations. *J. Phys. Chem. C* **114**, 14907-14914 (2010).
10. Bloch, E. D., Queen, W. L., Krishna, R., Zadrozny, J. M., Brown, C. M., Long, J. R. , *Science* **335**, 1606-1610 (2012).
11. Bachman, J. E., Kapelewski, M. T., Reed, D. A., Gonzalez, M. I., Long, J. R. M(m-dobdc) (M = Mn, Fe, Co, Ni) Metal-organic frameworks as highly selective, high-capacity adsorbents for olefn/parafn separations. *J. Am. Chem. Soc.* **139**, 15363-15370 (2017).
12. Lamia, N., Jorge, M., Granato, M. A., Almeida Paz, F. A., Chevreau, H., Rodrigues, A.

E. Adsorption of propane, propylene and isobutane on a metal-organic framework: molecular simulation and experiment. *Chem. Eng. Sci.* **64**, 3246-3259 (2009).

13. van den Bergh, J., Gucuyener, C., Pidko, E.A., Hensen, E.J., Gascon, J., Kapteijn, F. Understanding the anomalous alkane selectivity of ZIF-7 in the separation of light alkane/alkene mixtures. *Chem.-Eur. J.* **17**, 8832-8840 (2011).
14. Chen, Y., Qiao, Z., Lv, D., Duan, C., Sun, X., Wu, H., Shi, R., Xia, Q., Li, Z. Efficient adsorptive separation of $C_3H_6$ over $C_3H_8$ on flexible and thermoresponsive CPL-1. *Chem. Eng. J.* **328**, 360-367 (2017).
15. Wang, X., Krishn, R., Li, L. et al. Guest-dependent pressure induced gate-opening effect enables effective separation of propene and propane in a flexible MOF. *Chem. Eng. J.* **346**, 489-496 (2018).
16. Yu, M-H., S, B., F, D. et al. Enhanced Gas Uptake in a Microporous Metal-Organic Framework via a Sorbate Induced-Fit Mechanism. *J. Am. Chem. Soc.* **141**, 17703-17712 (2019).
17. Li, L., Lin, R-B., Wang, X. et al. Kinetic separation of propylene over propane in a microporous metal-organic framework. *Chem. Eng. J.* **354**, 977-982 (2018).
18. Liang, B. et al. An Ultramicroporous Metal-Organic Framework for High Sieving Separation of Propylene from Propane. *J. Am. Chem. Soc.* 142, 17795-17801 (2020).